MASTER

Dip coating film impinged by a gas jet

van der Boog, R.P.M.

Award date:
2018

Technische Universiteit
Eindhoven
University of Technology

Department of Applied Physics

Dip coating film impinged by a gas jet

Master Thesis

R.P.M. van der Boog

Supervisors:
F. Toschi
E. van Vliet
M. Duran Matute
H. Gelderblom
E.H. van Brummelen

First version

Eindhoven, October 2018

Abstract

Thin film flows are a classical fluid dynamics problem. One example is dip coating problems where the thin film flow is responsible for the coating during the vertical withdrawal of a plate from a reservoir (at sufficiently high speeds). Numerous experiments and numerical studies regarding this problem can be found in literature [20], as dip coating is widely used in industrial coating applications because of its simplicity and effectiveness. Additionally, the physics of dip coating is also relevant to several other common problems such as film entrainment retention.

In this thesis a numerical approach is employed in order to study dip coating problems, using the CFD software Gerris. Gerris is an open source code based on the volume of fluids methods with adaptive grid refinement capabilities. The software features a surface tension implementation and contact line dynamics based on the Cox-Voinov model in combination with local relaxation of the no-slip boundary condition.

As a first step the software is validated in situations where the physics of surface tension and of contact line dynamics play an important role. Amongst the case studies there are: a static meniscus rise, dip coating problem and the modelling of a gas jet. Additionally, novel research is performed relating the influence of an impinging jet on a film flow. The results reveal the dynamics of film thinning at the jet impact zone, accompanied with fluid build-up prior to this region. The relation between film thinning and both jet and wall velocities are investigated by means of a parameter sweep. The results found, indicate that the film thickness, e_j, decays as $e_j \propto \mathrm{Re_j}^{-2.41}$, where $\mathrm{Re_j}$ is the jet Reynolds number.

Contents

List of symbols

CFD	Computational Fluid Dynamics
CFL	Courant-Friedrichs-Lewy
CSF	Continuum Surface Force
FVM	Finite volume method
HF	Height Functions
PLIC	Piecewise Linear Interface Calculation
VoF	Volume of Fluid

Ca	Capillary number
$\mathrm{Ca_{cr}}$	Critical capillary number
Ca^*	Relative capillary number
CFL	CFL (or Courant) number
Fr	Froude number
Ma	Mach number
Re	Reynolds number
$\mathrm{Re_j}$	Reynolds number of the jet

γ	Surface tension
γ_{ls}	Surface tension of liquid-solid phase
γ_{sv}	Surface tension of solid-vapor phase
γ_{lv}	Surface tension of liquid-vapor phase
δ	Kronecker delta
ρ	Density
ρ_l	Density of liquid phase
ρ_g	Density of gas phase
θ	Angle
θ_A	Advancing angle
θ_D	Dynamic angle
θ_E	Equilibrium angle
θ_R	Rectraction angle
κ	Curvature
μ	Viscosity
μ_l	Viscosity of liquid phase
μ_g	Viscosity of gas phase
τ	Viscous stress tensor

A	Surface area
E	Energy
e	Film thickness
e_j	Film thickness after jet
e_{ll}	Thickness of Landau-Levich film
e_r	Ridge film thickness
F	Force per unit length
$\vec{g}$	Gravity vector
h	Meniscus height
L	Characteristic length scale
l	Macroscopic length scale
l_c	Capillary length
l_0	Microscopic length scale
p	Pressure
p_l	Pressure in liquid phase
p_v	Pressure in vapor phase
Q	Heat source
Q_{cl}	Flux at the contact line
Q_j	Flux at the ridge jump
Q_{ll}	Flux in the Landau-Levich film
$R_{1,2}$	Radii in perpendicular directions
s	Curvilinear coordinate
$\vec{q}$	Heat flux
T	Fluid tracking function
t	Time
U	Characteristic velocity scale
u, v	Velocity components
U_{cl}	Contact line velocity
U_j	Ridge jump velocity
U_p	Plate velocity
$\vec{u}$	Velocity vector
W	Work
x, y	Cartesian coordinates

Chapter 1

Introduction

Liquids wetting solids can be seen everywhere in daily life. By drinking from a glass of water or watching rain droplets moving down a window. Even though the relevant hydrodynamics of these phenomena are generally well understood, the dynamics at the contact line, which is the line separating wet regions from dry regions, presents still aspects in need for deeper understanding. Mainly, this is due to the vast range of scales present, as, in this type of flow problems, macroscopic fluid descriptions are influenced by the dynamics of molecules, responsible for contact line motion. At the contact line, classical macroscopic boundary conditions cease to be applicable, as molecular dynamics allows fluid particles to freely move along the boundary, restricted by intermolecular forces. The multiscale nature of the flow problem description at the contact line makes a description based on macroscopic equations alone difficult and consequently difficult for applicability in standard Computational Fluid Dynamics (CFD) tools. Numerically, a macroscopic description is desired capable of incorporating molecular dynamic effects in macroscopic fluid equation solvers (ranging from accurate contact line angle models to methods to resolve for shear stress singularities by local relaxation of no-slip boundaries [2, 19]).

In this work, one particular case of wetting is discussed, namely dip coating, also better known as the Landau-Levich problem. The problem describes entrainment of a thin film when a plate is extracted vertically from a reservoir at sufficient speed. A description of the phenomenon, is discussed in the pioneering work of Landau and Levich [14] dating back to 1942 and Derjaguin [8] in 1943. The papers are of particular interest regarding the predicted film thickness, especially useful for industrial applications such as dip-coating. The problem is a much researched subject, with experiments [9, 16, 15, 17, 21] and variations including temperature [6] and non-newtonian fluids have been performed [1].

In this work, a numerical study of the dip coating film entrainment problem is performed by means of computational simulations, followed by novel research of film thinning and contact line retention by applying an impinging jet on the film. In Chapter 2, the fundamental physics of thin film fluid dynamics is described, with emphasis on surface tension and contact line dynamics. Thereafter a few test cases are studied: the static meniscus rise in contact to a boundary wall, the dip-coating problem, and the description of a gas jet (that will be used later to impinge a thin film). In Chapter 3 details are provided on Gerris, the open source CFD software package used, with emphasis on the implementation of molecular phenomena using macroscopic descriptions. Finally, validation models are discussed in Chapter 4, confirming that Gerris is able to properly simulate contact line dynamics in multiphase flows, allowing to combine the case studies to research film thinning of entrained dip coating films.

Chapter 2

Theoretical background

In this chapter, the fundamental laws of fluid dynamics are reviewed, followed by molecular interactions and consequences thereof. Afterwards, the relevant dimensionless numbers are introduced and their use in similitude systems explained. Finally, a theoretical description of the models simulated is given.

2.1 Conservation laws

Any closed system is restricted to behave according to the mass, force, and energy balance. In differential form these equations are, respectively:

$$\frac{\partial \rho}{\partial t} + \nabla \cdot (\rho \vec{u}) = 0 \tag{2.1}$$

$$\frac{\partial \rho \vec{u}}{\partial t} + \nabla \left(\rho \vec{u} \vec{u}\right) = -\nabla p + \nabla \cdot \overline{\overline{\tau}} + \rho \vec{g} \tag{2.2}$$

$$\frac{\partial \rho E}{\partial t} + \nabla \left(\rho \vec{u} E\right) = -\nabla \cdot p \vec{u} + \nabla \cdot \left(\overline{\overline{\tau}} \cdot \vec{u}\right) + \rho \vec{u} \cdot \vec{g} + \frac{\partial Q}{\partial t} - \nabla \cdot \vec{q} \tag{2.3}$$

The first equation is known as the continuity equation, where t is time, ρ the density and $\vec{u}$ the velocity vector of components (u, v). The second equation is the force balance, including the pressure p, the stress tensor τ, and gravity $\vec{g}$. The third equation is the energy balance with E the energy, Q the heat source or sink and $\vec{q}$ the heat flux. In this work, there are no heat sources and the systems are assumed to be isothermal. Therefore, the energy balance equation (2.3) can be omitted for theoretical analysis and numerical models.

Equation (2.2) can be notoriously difficult to solve analytically in its general form. It can be simplified by assuming the fluids to be incompressible, an assumption that is valid for fluid velocities much lower than the speed of sound of that medium, i.e. $\mathrm{Ma} << 1$ as per equation (2.14). Also, there is no phase change, as evaporation of fluid and condensation of gas are neglected in this work. Mathematically, incompressibility ($\rho = constant$) allows equation (2.1) to be rewritten as:

$$\nabla \cdot \vec{u} = 0 \tag{2.4}$$

Implementation of this equation in equation (2.2) allows to rewrite it as:

$$\rho \frac{\partial \vec{u}}{\partial t} + \rho \vec{u} \cdot \nabla \vec{u} = -\nabla p + \mu \nabla^2 \vec{u} + \rho \vec{g} \tag{2.5}$$

where the second term on the right hand side is simplified by assuming $\mu = const$. This last condition is true for Newtonian fluids, such as water and air. The CFD flow solver used, solves equation (2.5) for each fluid component using the volume of fluid method, with an additional term modeling the surface tension. Details on the numerical model will be further elaborated in Chapter 3.

2.2 Surface tension

Small scale systems such as those discussed in this work are commonly dominated by surface tension. In this paragraph, an introduction to the phenomenology of surface tension is given using the example of a liquid-gas system together with its implications to microfluidic flows.

2.2.1 Physical origin

The physical origin of surface tension lies in the cohesive attraction between molecules in a fluid. In the bulk of the fluid, particles are in equilibrium due to an even force on all sides. At the liquid-vapor interface, however, this is not the case. Here the liquid attraction is weaker at the vapor side, yielding a net force into the liquid[1]. A schematic representation is shown in Figure 2.1.

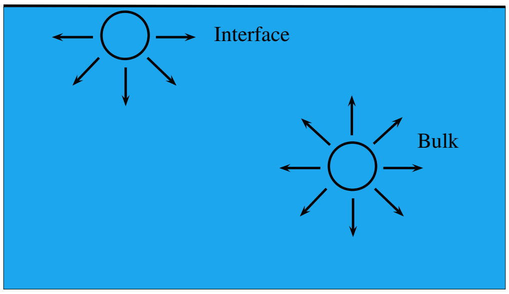

Figure 2.1: Schematic representation of an half space with a liquid-vapor interface at the top side. In the bulk the (right hand side) molecules are attracted equally in all directions, while at the surface, (left hand side) molecules experience a net attraction into the halfspace.

Due to the residual inward force the fluid tends to a minimal surface area. In continuum physics, this phenomena is described using the macroscopic concept of surface tension, which in mathematical form can be described as:

$$\delta W = \gamma \mathrm{d}A \tag{2.6}$$

where δW is the work required to change the surface area. Hence the dimensional units of surface tension are $\mathrm{J/m^2}$ or $\mathrm{N/m}$.

2.2.2 Laplace pressure

Intermolecular cohesive forces create an internal pressure in the fluid. At the interface, this leads to a pressure jump, depending on the shape of the interface, as the shape determines the net pulling force of individual molecules. The consequence is illustrated in Figure 2.2, as shown by the illustration, spherically shaped droplets are missing additional cohesive forces for molecules at the interface, yielding a larger inward force. In the fluid this reveals itself as a difference in pressure between the liquid and gas phases. This results in an extension of equation (2.6) [12]:

$$\delta W = -p_v \mathrm{d}V_v - p_l \mathrm{d}V_l + \gamma_{lv} \mathrm{d}A \tag{2.7}$$

---

[1] Adhesion forces (i.e. attraction between dissimilar molecule) between liquid and gas are not taken into account here.

In a stable equilibrium $\delta W = 0$ and equation (2.7) can be reduced to the well-known Young-Laplace equation:

$$\Delta p \equiv p_v - p_l = \kappa\gamma_{lv} = \gamma_{lv}\left(\frac{1}{R_1} + \frac{1}{R_2}\right) \tag{2.8}$$

where the curvature is denoted as κ, often approximated by circular shapes of radii R_1 and R_2 in 3D, and where Δp is known as the Laplace pressure, defined to be the difference between vapor and liquid pressure, respectively. The equation shows that convex shapes described with positive radii contain a positive Laplace pressure. The opposite is also true for concave surfaces, such as the one shown in Figure 2.2, where negative radii result in a negative Laplace pressure.

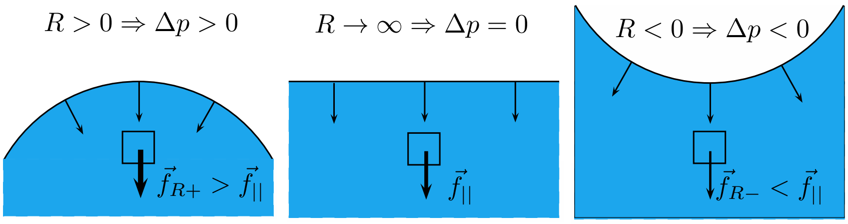

Figure 2.2: Schematic representation of a convex, halfspace and concave scenario respectively, with the gas side atop. The convex shape is defined to have a positive radius leading to a positive Laplace pressure. Elements, indicated by a square, close to the liquid interface experience a net downward force. The magnitude of this force is determined by the amount of liquid elements between the visualized square element and the interface (at equal vertical distance).

2.2.3 Static contact line

Near a boundary wall, at the static contact line, cohesive and adhesive forces balance (attractive forces between, respectively, similar and dissimilar molecules), leading to a stationary state described by Young's equation:

$$\gamma_{lv}\cos(\theta_E) + \gamma_{ls} = \gamma_{sv} \tag{2.9}$$

with γ_{ls}, γ_{sv}, and γ_{lv} (the latter also referred to as γ from here onwards) the surface tensions of liquid-solid, solid-vapor, and liquid-vapor interfaces, respectively. The apparent contact angle θ_E is the angle at macroscopic level as shown in Figure 2.3. In case there is no angle $\theta_E = 0$, the liquid is said to be perfectly or completely wetting the solid surface. When the angle is $\theta > 0$, the liquid is partially wetting the solid surface, being wetting for $\theta < 90°$, and non-wetting for $\theta > 90°$. The nomenclature corresponds to hydrophilic and hydrophobic, respectively, if the liquid in question is water.

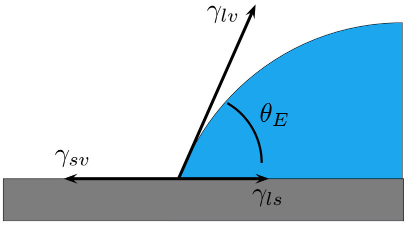

Figure 2.3: Schematic representation of the surface tension forces involved in the Young's equation (2.9) at the (triple) contact line of a droplet.

The contact angle, as described in equation (2.9), is only valid for perfectly flat and homogeneous solid surfaces. In practice, even the cleanest surfaces are not perfect [21], leading to contact line hysteresis, such that static state can be achieved in a range of contact line angles $\theta_R < \theta_E < \theta_A$. With $\theta_{R,E,A}$ the receding, equilibrium and advancing contact line angles, respectively, owing their names to the direction of movement of the contact line.

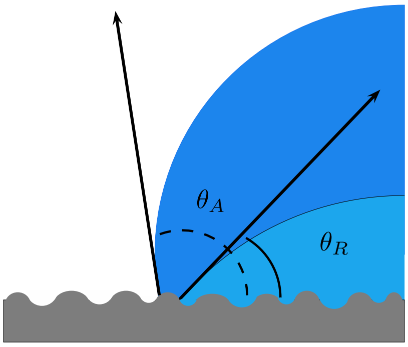

Figure 2.4: Schematic representation of stagnant droplets revealing the hysteresis phenomena. Locally the angles are equal to θ_E close to the surface, yet reveal themselves as θ_R and θ_A from afar due to surface roughness.

2.2.4 Contact line dynamics

Macroscopic fluid problems are usually assumed to have a no-slip boundary condition. With this boundary condition, liquid near the contact line is retained at a fixed position with respect to the wall. This leads to a singularity problem, where an infinite force would be required to move the contact line [13]: implying that it would be impossible to extract a submerged object from a liquid reservoir. This paradox indicates that macroscopic no-slip boundary conditions are not valid at the smallest scale near the contact line. Instead, at atomic scales, contact line motion is properly described only by molecular dynamics, allowing the contact line at the smallest scale to move in either direction based on the net force applied. In case of no hysteresis, the force per unit length F becomes apparent when the contact line angle is different from the equilibrium angle [10]:

$$F(\theta_D) = \gamma \left(\cos\,\theta_E - \cos\,\theta_D\right) \tag{2.10}$$

Where θ_D is the dynamic angle at which movement of the contact line will occur. When hysteresis is included, the equilibrium angle θ_E is replaced by either θ_A or θ_R in the respective cases that $\theta_D > \theta_A$ or $\theta_D < \theta_R$ [12]. A schematic overview of contact line motion is shown in Figure 2.5.

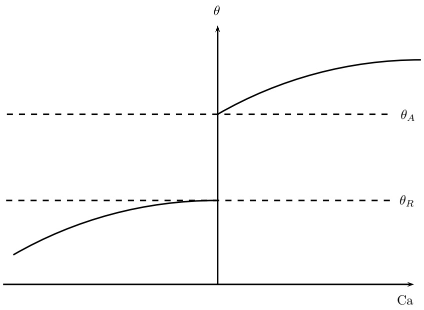

Figure 2.5: Schematic of contact line hysteresis, with on the left hand side the velocity of a retracting contact line angle and, on the right side, the advancing one. The region on the vertical axis is known as static contact line hysteresis, whereas the outer regions are known as dynamic contact line hysteresis. The horizontal axes represents the velocity of liquid relative to the substrate shown by the dimensionless Capillary number $Ca = \frac{\mu U}{\gamma}$. The graph is reproduced from [10].

2.3 Dimensionless numbers and similitude

Dimensionless numbers play an important role in analyzing the physical behavior of systems. It can be used to determine the dominant physical phenomena or to study geometrical and dynamical similar system by means of parameter rescaling. Rescaling of system parameters is repeatedly used throughout this work to prevent numerical artifacts in simulation results. The rescaling of system parameters is elaborated after an introduction to the most relevant dimensionless numbers of this work.

2.3.1 Dimensionless numbers

The Reynolds number, Re, is the ratio of inertial to viscous forces in a fluid. It is defined as:

$$\mathrm{Re} \equiv \frac{\rho U L}{\mu} \tag{2.11}$$

with L and U being the characteristic length and velocity scale of the system and, ρ and μ the density and viscosity fluid properties, respectively. For large values of the Reynolds number the fluids inertia dominates and the flow becomes turbulent, whereas smaller values of the Reynolds number are said to be laminar. As it turns out, all cases in this work are within the laminar regime, with the gas jet being no exception.

The capillary number, Ca, indicates the ratio of viscous forces versus surface tension force and is defined as:

$$\mathrm{Ca} \equiv \frac{\mu U}{\gamma} \tag{2.12}$$

with γ the surface tension. The capillary number is relevant for fluid interfaces as commonly encountered in multiphase fluids. In this work the capillary number is particularly relevant to contact line movement and the deformation of interfaces close to the triple line.

The Bond number Bo (or Eötvös number) compares the relative importance of gravity to surface tension:

$$\mathrm{Bo} = \frac{\rho g L^2}{\gamma} \tag{2.13}$$

with g gravity and is again a useful quantity for the analysis of thin films and droplets regarding their shape.

The Mach number, Ma, indicates the velocity compared to the speed of sound, c, of the medium:

$$\mathrm{Ma} \equiv \frac{U}{c} \tag{2.14}$$

The Mach number substantiates incompressibility assumptions made in the CFD solver, requiring Ma << 1 for incompressibility assumptions to be applicable.

The CFL number (or Courant number), named after Courant-Friedrichs-Lewy, is an important dimensionless number in numerical computations:

$$\mathrm{CFL} \equiv \frac{U\Delta t}{\Delta x} \tag{2.15}$$

with Δt the time step, Δx the mesh size and U the velocity of information. A CFL > 1 would essentially allow information to migrate over distances larger than a single node or mesh size. This can, for example, be detrimental to numerical solutions of traveling waves. It is common practice to enforce CFL < 0.7 in microfluidic simulations, although Gerris by default uses CFL < 0.5.

2.3.2 Similitude

Similitude is an important application of non-dimensional numbers. If similitude between systems is obtained, a system can be accurately solved by a smaller or larger physical model, with the exact same (rescaled) solution as the original system. The required conditions to obtain similitude are [5]: geometrical similarity and dynamical similarity. Geometrical similarity is present when the physical model is an exact scaled replica of the original system. Dynamical similarity is achieved when forces and velocities in the system are the scaled equivalence of those in the physical model, i.e. forces and velocities are also rescaled accordingly. Conditions for dynamical similarity are met if the dimensionless numbers of both the system and physical model are equal. This statement is supported by the dimensionless form of the Navier-Stokes equation (2.5). In order to write the dimensionless Navier-Stokes equation, the following definition of dimensionless parameters is used:

$$\begin{array}{llll} t' \equiv \frac{U_0}{L}t, & \rho' \equiv \frac{\rho}{\rho_0} & p' \equiv \frac{\mu U_0}{L}p & \nabla' \equiv \nabla L \\ U' \equiv \frac{U}{U_0} & \mu' \equiv \frac{\mu}{\mu_0} & g' \equiv \frac{g}{g_0} & \end{array}$$

with U_0 and L a characteristic velocity and lengthscale of the system, respectively, and where the fluid has a density ρ_0, and a viscosity μ_0, subjected to a gravitational force of g_0. By substitution in the Navier-Stokes equation (2.5) and omitting the primes, the following dimensionless form can be obtained:

$$\mathrm{Re}\left[\frac{\partial}{\partial t}\rho\vec{u} + \rho\vec{u}\cdot\nabla\vec{u}\right] = -\nabla p + \mu\nabla^2\vec{u} + \frac{\mathrm{Bo}}{\mathrm{Ca}}\rho\vec{g} \tag{2.16}$$

The solution of the dimensionless Navier-Stokes equation is only dependent on the dimensionless numbers: Reynolds number Re, Bond number Bo, and capillary number Ca. Hence a fluid system is mathematically indistinguishable for any physical model if the dimensionless numbers are equal and geometrical similarity is present. Thus any length scale of a given geometry with equal dimensionless numbers lead to the same result.

The concepts of similitude systems are used for conducting experiments which are infeasible otherwise, for example aerodynamic tests of ships and airplanes, due to their large size. The concept is however also convenient in CFD, as it allows to change fluid properties without changing the result (as long as dimensionless numbers are equal). In this work, similitude of systems is used to reduce artifacts in numerical calculations of the interface. A detailed explanation of similitude necessity is discussed in Chapter 3.

2.4 Dip coating

This paragraph contains a brief recall of the most important concepts regarding liquid-solid interactions as due to the fundamental physics mentioned before. Various case studies will be discussed: the first scenario is the static interaction between a liquid and a solid, the second is the dip coating problem (i.e. the extraction of a plate from a liquid reservoir), finally, a short description of laminar jet physics is given, together with a formulation of the film thickness when applying an impinging jet on a dip coating setup. The cases studied in this paragraph will be simulated for validation purposes and results are reported in chapter 4.

2.4.1 Static capillary rise

A stagnant liquid in contact with a vertical wall develops an equilibrium contact line angle balancing the surface tensions, as described by equation (2.9). This means that the fluid interface is displaced until the equilibrium angle is reached. A meniscus is formed for wetting fluids, i.e. $\theta_E < 90°$, and the capillary rise height can be calculated from equation (2.5). In the following analysis, the fluid velocity is $\vec{u} = (0, 0)$, resulting in a solution for a static meniscus, where the surface tension and gravitational forces balance in static equilibrium. Implementing $\vec{u} = (0, 0)$ in equation (2.5):

$$0 = -\nabla p_{l,v} + \rho_{l,v}\vec{g} \tag{2.17}$$

The solution of equation (2.17) results in a hydrostatic pressure equation $p_{l,v} = -\rho_{l,v} g y + C_{l,v}$ for both liquid and vapor phases. The integration constants, $C_{l,v}$, can be found by defining $y = 0$ at the liquid-gas interface far away from the wall, where the curvature $\kappa = 0$. Here, the Laplace pressure is negligible, allowing to connect the equations of liquid and gas such that $C_l = C_v = p_{amb}$, the ambient pressure.

In contrast, close to the wall the curvature is not negligible and enforces the use of the Laplace pressure equation 2.8 such that $p_l + \kappa\gamma = p_v$. Substitution of the previously found hydrostatic pressure terms results in:

$$-\Delta\rho g y + \kappa\gamma = 0 \tag{2.18}$$

with $\Delta\rho \equiv \rho_l - \rho_v$. The height of the capillary rise can be determined from equation 2.18 by describing the curvature in curvilinear coordinates [12]:

$$\kappa = \frac{\mathrm{d}\theta}{\mathrm{d}s} \tag{2.19}$$

where the angle θ and the curvilinear coordinate s are defined in Figure 2.6. Next to this, a trigonometrical argument can be used to show that the linearized curve along s equals $-\frac{\mathrm{d}y}{\mathrm{d}s} = \cos\theta$. By substitution of the trigonometrical argument in equation (2.19), in combination with equation (2.18), this leads to:

$$\Delta\rho g y + \gamma\frac{\mathrm{d}\theta}{\mathrm{d}y}\cos\theta = 0 \tag{2.20}$$

Solving this differential equation provides the solution for the meniscus height, h, as a function of the equilibrium angle, θ_E:

$$\gamma\sin\theta + \frac{1}{2}\Delta\rho g y^2 = C_1 \tag{2.21}$$

Where the constant C_1 can be determined by inserting the boundary condition $\theta = 90°$ with a corresponding height of $y = 0$. The meniscus height $h = y(\theta)$ can now be found by inserting the equilibrium angle at the wall $\theta = \theta_E$:

$$h(\theta_E) = \sqrt{2}l_c\sqrt{1 - \sin\theta_E} \tag{2.22}$$

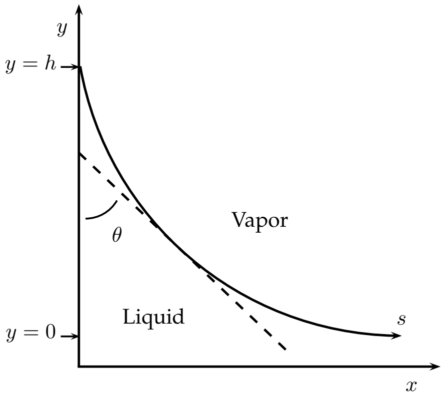

Figure 2.6: The curvature of a meniscus in a fluid described in curvilinear coordinate s (coordinate along the surface interface) and angle θ.

where $l_c \equiv \sqrt{\frac{\gamma}{\Delta\rho g}}$ is the capillary length. This characteristic length-scale will return quite often throughout this work and is especially useful in descriptions of systems where surface tension and gravitational forces balance.

Coincidentally, it is also possible to obtain an analytical solution for the entire meniscus. The procedure to achieve this uses the definition of the curvature κ in cartesian coordinates:

$$\kappa = \frac{\frac{\mathrm{d}^2 y}{\mathrm{d}x^2}}{\left[1 + (\frac{\mathrm{d}y}{\mathrm{d}x})^2\right]^{3/2}} \tag{2.23}$$

Combined with equation (2.18), this equation can be solved into an explicit relation for the curve, as shown by [12] [22], here only the final result is reported:

$$x - x_0 = l_c \cosh^{-1}\left(\frac{2l_c}{y}\right) - 2l_c\left(1 - \frac{y^2}{4l_c^2}\right)^{1/2} \tag{2.24}$$

with x_0 the distance such that $y = h$ at $x = 0$.

2.4.2 Film pulling

In the case of a slow moving wall, in the direction of positive y, the static shape of the meniscus becomes deformed due to the flow induced by the moving wall. The contact line angle is decreased to a dynamic contact line angle, θ_D, by the induced upward flow and will move to the equilibrium angle θ_E. The equilibrium angle can however not be maintained due to the moving wall. Therefore, a new stationary solution is obtained with a contact line velocity equal to the wall velocity.

Above some critical wall velocity, stationary solutions cease to exist as the contact line velocity is unable to match the speed of the wall. Entrainment of liquid will then coat the wall with a liquid film, also known as a Landau-Levich film. Several interesting phenomena occur in this film, it is therefore convenient to break up the film into different regimes and discuss them separately. First a description of an infinite flat thin film is given, followed by the film front, and finally the transition zone in between the thin film and the film front will be discussed.

Film flow

A vertical wall moving in upward direction with a flat fluid entrained with thickness e is shown in Figure 2.7a. The wall induces an upward flow in the liquid due to the no-slip boundary condition at the wall, while the gravitational body force acts downward. The flow is described by the Navier-Stokes equation (2.5). A steady state solution exists, because there is no time dependent force, indicating that the solution is both time and vertically independent, $\frac{\partial}{\partial t} = 0$, $\frac{\partial}{\partial y} = 0$. Also, the film is flat and no horizontal forces are present, such that the horizontal velocity is zero, $u = 0$. Applying this to the Navier-Stokes equation (2.5) leads to:

$$0 = -\frac{\mathrm{d}p}{\mathrm{d}x} \tag{2.25.a}$$

$$0 = -\frac{\mathrm{d}p}{\mathrm{d}y} + \mu\frac{\mathrm{d}^2 v}{\mathrm{d}x^2} - \rho g \tag{2.25.b}$$

Evidently, the pressure in the horizontal direction is constant, as the gradient in the horizontal direction is zero (equation (2.25a)) and there is no curvature in the flat film. What remains is equation (2.25b), which is the ordinary differential form of a Poiseuille flow. The flow profile can be solved analytically using two applicable boundary conditions. The first boundary condition is the velocity near the plate moving at the same speed, $v(x = 0) = U_p$. The second boundary condition is present at the free interface, where the viscous stress is zero or at least negligible in case of a gas. This means that the gradient of the velocity is zero at the interface, $\frac{\mathrm{d}v(x=e)}{\mathrm{d}x} = 0$, i.e. the velocity at the interface is continuous from liquid to gas. Solving equation (2.25) using the boundary conditions gives the final velocity profile in the thin film:

$$v(x) = \frac{\rho g}{\mu}\left(\frac{x^2}{2} - ex\right) + U_p \tag{2.26}$$

with e the film thickness.

Equation (2.26) also allows the determination of a maximum stable film thickness since negative velocities near the interface cannot contribute to a thicker film in case the source of liquid is a reservoir (i.e. a starting point). Hence, a theoretical maximum film thickness occurs when $v(x = e_m) = 0$, resulting in:

$$e_m = \sqrt{\frac{2\mu U_p}{\rho g}} = \sqrt{2} l_c \mathrm{Ca}^{1/2} \tag{2.27}$$

with the relevant capillary number, $\mathrm{Ca} = \frac{\mu U_p}{\gamma}$, and $l_c = \sqrt{\frac{\gamma}{\rho g}}$ being the capillary length. Put differently, if a film exceeds the thickness of equation (2.27), the velocity at the interface will be negative.

2.4.3 Film thickness

The discussed film flow applies to the ideal case of an infinite film, whereas a dip coating film starts in a liquid reservoir and ends in the film front. In this paragraph, the influence of the liquid reservoir and of the moving contact line with respect to the dip coating film are discussed. Starting with the film thickness withdrawn from a liquid reservoir.

Landau-Levich film

The solution for the film thickness is found by Landau-Levich-Derjaguin and described in their famous paper [14, 8]. In what follows, a derivation of the Landau-Levich-Derjaguin film thickness is given based on [16].

In the work of Landau, Levich, and Derjaguin, it is shown that the high curvature in the meniscus and the viscous stress induced by the moving wall cause surface tension and viscous forces to dominate the flow over gravitational forces. Therefore gravity can be neglected in this analysis. Furthermore, in the case $\mathrm{Ca} << 1$ the curvature can be approximated by $\kappa \approx \frac{\mathrm{d}^2 e}{\mathrm{d}y^2}$, resulting in a Laplace pressure of $\Delta p = -\gamma\frac{\mathrm{d}^3 e}{\mathrm{d}y^3}$. Substitution of the Laplace pressure in equation (2.25.b) and neglecting gravity leads to a balance between surface tension and viscosity forces:

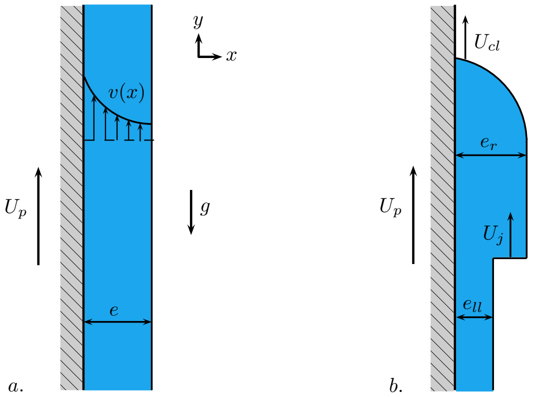

Figure 2.7: a) Infinite plate moving in upward direction with velocity U_p and a liquid film entrained subjected to a gravitational pull. The resulting velocity profile in the liquid is indicated by the curve at $v(x)$, with the dotted line as a reference. The film thickness is denoted by e. b) Simplified overview of the liquid film front build-up due to the difference in velocity of the plate, U_p, and the contact line, U_{cl}. The ridge is elongated in vertical direction due to increasing build-up in time. Here, the transitional zone from the film to the ridge is estimated to be sharp-edged, moving with a velocity U_j. The thickness of the front ridge and the Landau-Levich film are denoted by e_r and e_{ll}, respectively.

$$-\gamma\frac{\mathrm{d}^3e}{\mathrm{d}y^3}=\mu\frac{\mathrm{d}^2v}{\mathrm{d}x^2} \tag{2.28}$$

The equation can be solved to reveal the velocity profile at the top of the meniscus, using the same boundary conditions as the regular film flow (equation (2.26)). Namely, the first being a stress-free boundary at the interface $\frac{\mathrm{d}v}{\mathrm{d}x}(x=e)=0$. And secondly, fluid in contact with the plate moving at the same speed due to a no-slip boundary condition, $v(x=0)=U_p$. The flow profile then becomes:

$$v(x)=-\frac{\gamma}{\mu}\frac{\mathrm{d}^3e}{\mathrm{d}y^3}\left(\frac{x^2}{2}-ex\right)+U_p \tag{2.29}$$

valid in the meniscus shape. In case the plate velocity is significantly larger than the critical velocity for entrainment, it can be shown that the velocity of (2.26) is approximately equal to the plate velocity for thin films. Implementing this in a flux balance between the meniscus velocity profile and the thin film flow:

$$U_pe+\frac{\gamma}{3\mu}\frac{\mathrm{d}^3e}{\mathrm{d}y^3}e^3=U_pe_{ll} \tag{2.30}$$

This equation can be made dimensionless by substitution of $E=e/e_{ll}$, with e_{ll} the Landau-Levich film thickness, and $Y=y/\lambda$, where $\lambda\equiv e_{ll}/(3\mathrm{Ca})^{1/3}$:

$$\frac{\mathrm{d}^3E}{\mathrm{d}Y^3}=\frac{1-E}{E^3} \tag{2.31}$$

By definition, the film thickness far from the meniscus should be equal to the Landau-Levich film thickness, $e(y\to\infty)=e_{ll}$. In dimensionless form, this boundary condition is written as $E(Y\to\infty)=1$. A solution can thus be found by expansion in a first order power series $E=1+\epsilon(Y)$, where only small variations are allowed, i.e. $\epsilon(Y)<<1$:

$$\frac{\mathrm{d}^3\epsilon}{\mathrm{d}Y^3}=\frac{-\epsilon}{1+\epsilon}\approx-\epsilon \tag{2.32}$$

This differential equation has an exponential solution, $\epsilon = \alpha \exp[-Y]$, with α a measure of the curvature in the film. All that remains is to connect the exponential solution to the dynamic meniscus. In the work of Landau and Levich, the dynamic meniscus is assumed to be equal to the static meniscus solution, the exponential solution can then be connected to the static meniscus shape at equal curvature. This requires the height of the meniscus at an equilibrium contact line angle of $\theta_E = 0$ (liquid-liquid interaction by itself is perfectly wetting), found to be $h(\theta_E = 0) = \sqrt{2}\ l_c$ (equation (2.22)). Furthermore, it was found that the curvature of both solutions match at a value of 0.644. Hence the two solutions can be matched at this position. Ultimately leading to the desired film thickness [14, 16, 12, 20, 21]:

$$e_{ll} \approx 0.644\sqrt{2} l_c \mathrm{Ca}^{2/3} \approx 0.945\ l_c \mathrm{Ca}^{2/3} \tag{2.33}$$

with the capillary length $l_c = \sqrt{\frac{\gamma}{\rho g}}$, and capillary number $\mathrm{Ca} = \frac{\mu U_p}{\gamma}$. The Landau-Levich equation (2.33) is confirmed by experiments.

Front ridge

At the film front, movement of the wall will reduce the equilibrium contact line angle to some dynamic contact line angle, $\theta_D < \theta_E$. The contact line then starts to move in downwards direction relative to the plate, towards the equilibrium contant line angle. The velocity of the contact line relative to the reservoir is now smaller than the plate velocity, $U_p > U_{cl}$, and shown by U_{cl} in Figure 2.7b. A velocity difference between the contact line and the plate velocity becomes apparent and is called the slip velocity. A dimensionless number can be defined to reflect the slip velocity. This dimensionless number is the relative capillary number, defined as $\mathrm{Ca}^* \equiv \frac{\mu}{\gamma}\left(U_p - U_{cl}\right)$ [21].

The slip velocity enforces a liquid build-up near the contact line due to mass conservation, visualized in Figure 2.7b. The liquid build-up develops in a front ridge due to the Poiseuille flow profile, distributing the liquid build-up along the film. In time, the redistribution of fluid causes a fixed shape and ridge thickness at the film front.

A relation between the ridge thickness, e_r, and the contact line velocity, U_{cl}, can be found by applying a mass balance in the ridge. For the fixed shape of the contact line this produces a volumetric flow rate of $Q = e_r U_{cl}$, whereas the flow rate in the ridge is the integral of the ridge flow, leading to a balance of:

$$e_r U_{cl} = \int_0^{e_r} v(x)\mathrm{d}x \tag{2.34}$$

Solving using the Poiseuille flow of equation (2.26) allows to derive a relation for the ridge thickness e_r:

$$e_r = \sqrt{\frac{3\mu}{\rho g}\left(U_p - U_{cl}\right)} = \sqrt{3} l_c \mathrm{Ca}^{*1/2} \tag{2.35}$$

In [21] it is implied that the ridge thickness is solely dependent on the equilibrium contact line angle. A consequence of this assertion would be that the relative capillary number is also solely dependent on the the equilibrium contact line angle, due to equation (2.35). Meaning that the slip velocity is independent of the plate velocity, i.e. Ca^* is independent of Ca. The experimental results found by [21] and simulations in this work indeed confirm this independence.

2.4.4 Flow in the transition zone

As previously mentioned in Figure 2.7, the transition zone is assumed to have a fixed shape. Fluid is accumulated here because the flow near the interface of the thinner film is moving faster than flow in the ridge. This velocity difference leads to a phenomenon known as a capillary shock, where accumulated capillary waves are retained to pass the transition zone by the velocity difference [6, 7, 21].

A relation between the transition velocity U_j, the thickness of the film and the ridge thickness can be found by applying a mass balance along the entire ridge, including the transition zone as displayed in Figure 2.7. This results in $Q_{ll} + Q_j - Q_{cl} = 0$, being the volumetric flow rate due to the Landau-Levich film Q_{ll}, ridge transition zone Q_j, and contact line Q_{cl}, respectively. The individual volumetric flow rates are:

$$Q_{ll} = \int_0^{e_{ll}} v(x)\mathrm{d}x \tag{2.36.a}$$

$$Q_j = \int_{e_{ll}}^{e_r} U_j \mathrm{d}x \tag{2.36.b}$$

$$Q_{cl} = \int_0^{e_r} U_{cl} \mathrm{d}x \tag{2.36.c}$$

with $v(x)$ the Poiseuille flow of equation (2.26). Substitution in the mass conservation results in the following dimensionless solution:

$$\frac{\mu U_j}{\gamma} = \mathrm{Ca} - \frac{e_r^2 + e_r e_{ll} + e_{ll}^2}{3l_c^2} \tag{2.37}$$

Providing the same result as found in [21].

2.4.5 Film thickness with an impinging jet

As discussed in paragraph 2.3.2, a flow problem is only dependent on the relevant dimensionless numbers. As such, the film thickness in a dip coating setup is a function of $e = f(\mathrm{Ca}, \mathrm{Re}, \mathrm{Bo}, \theta_E, l)$, with the capillary number Ca, Reynolds number Re, Bond number Bo, equilibrium contact line angle θ_E, and a relevant length scale l. However, in paragraph 2.4.3 it is found that the Landau-Levich film thickness is only dependent on the capillary number and capillary length, $e_{ll} = f(\mathrm{Ca}, l_c)$, while the ridge thickness is found to be dependent on the relative capillary number and capillary length $e_r = f(\mathrm{Ca}^*, l_c)$. Hence a more convenient way of writing the dependence of the film thickness would be $e = f(\mathrm{Ca}, \mathrm{Ca}^*, l_c)$.

In addition, implementing an impinging jet in the numerical dip coating requires an additional dependent parameter for the jet flow. This parameter is the Reynolds number of the jet, $\mathrm{Re_j}$, since the dimensionless Navier-Stokes equation in horizontal direction (perpendicular to gravity) is solely dependent on this dimensionless number:

$$\mathrm{Re_j}\left[\frac{\partial}{\partial t}\rho u + \rho u \cdot \nabla u\right] = -\nabla p + \mu \nabla^2 u \tag{2.38}$$

Implementation of a horizontal jet impinging a dip coating film is therefore expected to be a function of:

$$e_j = f(\mathrm{Ca}, \mathrm{Ca}^*, \mathrm{Re_j}, l_c) \tag{2.39}$$

where Ca determines the film flow for $\mathrm{Ca} > \mathrm{Ca_{cr}}$, Ca^* indicates the amount of slip between the plate and the contact line, $\mathrm{Re_j}$ determines the jet flow, and l_c the capillary length being a relevant length scale for the problem, as well as providing the influence of gravity. As previously discussed in paragraph 2.4.3, the relative capillary number is constant for a given equilibrium contact line angle and the capillary length is a constant value determined by fluid properties and gravity. Hence the only variables of the film thinning problem are the capillary number of the fluid and Reynolds number of the jet. The influence of these variables is investigated in paragraph 4.4 to further determine the thinned film thickness e_j dependency on these dimensionless numbers.

Chapter 3

Numerical methods

In this chapter the numerical methods beyond the computational fluid dynamic software Gerris are presented. The software is open source and able to solve for Euler, Stokes and Navier-Stokes equations amongst others. The program allows to solve for multiphase and multicomponent simulations containing molecular phenomena such as contact line dynamics and surface tension. Other useful features implemented are parallel computing and load balancing together with a simple mesh characteristic to Gerris.

3.1 Finite volume method

Gerris uses flow solvers of the Finite Volume Method (FVM) type. Similar to the finite difference and finite element methods, FVM computes values at discretized locations on the mesh. The difference of FVM is that the equations are computed as a flux through the surfaces of boundaries in discretized volumes. Because the outward flux is exactly equal to the inward flux of the adjacent volume, the method is a conservative one. However, due to implementation of multiphase interface computation the conservation of mass is lost at the interface.

Flow problems discussed in this work have low Mach numbers $\mathrm{Ma} << 1$ and are, by assumption, isothermal. Due to the former assertion, problems can be assumed incompressible ($\rho = \text{constant}$), allowing to deal with the Navier-Stokes equation only. The equation solved by Gerris is quite similar to equation (2.5) with an additional inclusion of a macroscopic description of surface tension:

$$\rho \frac{\partial \vec{u}}{\partial t} + \rho \vec{u} \cdot \nabla \vec{u} = -\nabla p + \mu \nabla^2 \vec{u} + \rho \vec{g} + \kappa \gamma \delta_s \vec{n} \tag{3.1}$$

with Kronecker δ_s indicating availability of surface tension only on the interface, and $\vec{n}$ the normal vector of the interface.

The fundamentals are thoroughly discussed in [18][19], while in the remainder of this chapter, only the most important features of Gerris will be briefly discussed.

3.2 Domain

A simulation domain is build using square boxes. The software allows to stack multiple boxes on top and alongside of each other, in order to create more complex model domains. Each individual boundary non-adjacent to other boxes allows to setup a boundary condition. In addition, Gerris allows to generate solid boundaries based on logical functions, perforating the domain to its desired shape or generating a negative of it when using the flip command. In contrast to box boundaries, solid boundaries only allow for global boundary conditions. Furthermore, solids cannot be used as open boundaries, limiting domain design flexibility.

3.3 Mesh

One of the main characteristic features of Gerris is its use of structured quad/octree grid meshes. This type of mesh retains the advantages of an uniform Cartesian grid, while allowing to locally refine the grid to a coarser or finer mesh. This adaptive refinement is, as the name implies, implemented in a dynamic manner and can be applied on any fluid property or function. The ease of implementation of a quad/octree mesh allows to re-mesh every time step with only a few percentages of additional computational runtime [4]. An example of the quad/octree mesh can be seen in Figure 3.1.

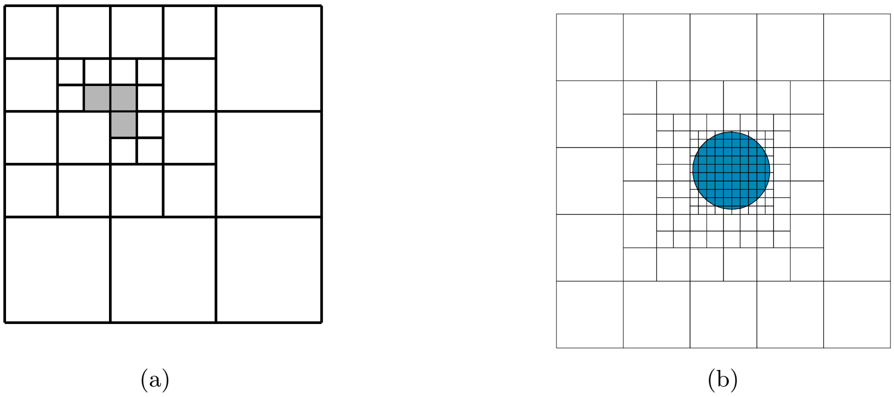

(a) (b)

Figure 3.1: a) Schematic representation of a quad/octree mesh around a small object. There are three levels of mesh sizes present. If, for instance, the object was refined two levels higher than the coarse outer cells, this would be the minimal cell configuration. b) Adaptive mesh refinement surrounding a droplet based on the VoF tracking function T. This particular example is captured from a simulation.

The grid size is set up in levels. Each level increases the amount of cells as a power of 2 in all directions for one particular box domain. Adaptive mesh refinement can be used to locally increase the level based on any internal function. With the only restriction that the mesh generator of a multilevel grid is restricted to one level difference with adjacent cells.

3.4 Volume of Fluid method

Multiphase and multicomponent simulations in Gerris can be realised using the Volume of Fluid method (VoF). The method introduces a characteristic function T to track fluids. For example, in this work $T = 0$ denotes the gas phase, whereas $T = 1$ is the liquid phase. Material properties of the fluids are applied based on value of T. For the density and viscosity this implies:

$$\rho = \rho_0 + (\rho_1 - \rho_0)\,T \tag{3.2.a}$$

$$\mu = \mu_0 + (\mu_1 - \mu_0)\,T \tag{3.2.b}$$

Allowing the material properties to vary throughout the domain based on T. In order to allow fluids to displace one another, a dynamic description of the tracking function is required, this is the advection equation for T:

$$\frac{\partial T}{\partial t} + \vec{u} \cdot \nabla T = 0 \tag{3.3}$$

Relevance of this equation is solely important to cells containing the interface between fluids, being the only position where $\nabla T \neq 0$ due to the incompressibility assumption.

3.5 Implementation of molecular phenomena

Both surface tension and contact line movement are molecular phenomena. However, Gerris only solves for the macroscopic fluid dynamics Navier-Stokes equation. To solve for both molecular phenomena, VoF, Height Functions (HF), Continuum Surface Force (CSF) and the Cox-Voinov model are used [2]. The following paragraphs contain a brief explanation of the basic principles.

3.5.1 Surface tension

In short, HF is used to determine a sharp interface [2][19]. The VoF tracking function T is exploited for this purpose by summing a column (or row) of T around the interface cell to obtain the height of the interface in that particular cell [2], this is either performed in vertical or horizontal direction. Effectively, this procedure results in an interface height approximation with an accuracy smaller than the cell size. The normal vector of the interface $\vec{n}$ can then be extracted using a finite difference scheme on the neighboring interface heights. Combining $\vec{n}$ and the cell centre heights allow reconstruction of the interface in that cell. The procedure is of the Piecewise Linear Interface Calculation (PLIC) type [2], and strongly benefits from small mesh sizes as it is first order accurate.

Near the domain boundaries, cells in (at least) one direction are absent. Here ghost cells are used with an interface set to the equilibrium angle θ_E of the boundary, used for the determination of the interface of a cell adjacent to the boundary. The method therefore acts as a boundary condition for the interface.

Furthermore, a finite difference scheme is used to determine the curvature by approximation of the first and second order derivative of the interface height and inserting it into equation (2.23). With both the surface interface and curvature known, surface tension can be implemented as shown in equation (3.1) by use of a discretized CSF method.

The above method converges with mesh refinement and should be less prone to spurious (or parasitic) currents [11][2] in comparison to other methods. Some other methods work in converse by determining the normal vector by evaluating ∇T. The spurious currents mentioned are numerical artifacts which are further elaborated in paragraph 3.6. A drawback of HF is that an object should not be fully contained by a mesh cell, as this will result in incorrect interface computations. In Gerris however, adaptive mesh refinement can be used to resolve this deficiency by applying additional mesh refinement.

3.5.2 Contact line dynamics

In general, viscous flow along a boundary is solved by applying a no-slip boundary condition. This contradicts with contact line movement along the boundary, leading to a singularity problem, as discussed in 2.2.4. Contact line movement is hence prohibited by the no-slip condition applied on the boundary. To resolve this, a local relaxation of the no-slip boundary condition is used to remedy the stress singularity at the contact line, based on the mesh size.

Furthermore, a model for advancing and receding contact lines is required. Gerris solves this by using a method based on the Cox-Voinov model [20]. The model relates the equilibrium angle, θ_E, and the capillary number to the dynamic angle, θ_D, of a moving contact line:

$$\theta_D^3 = \theta_E^3 - 9\mathrm{Ca}\ln\left(\frac{l}{l_0}\right) \tag{3.4}$$

where l is an outer macroscopic length such as the capillary length or domain size and l_0 a microscopic length related to molecular processes. The former can be determined from properties provided in the simulation. The latter is approximated as a fraction of the mesh size. A direct consequence is that the final outcome of a simulation becomes mesh and domain dependent [3]. Therefore attention must be paid when simulating a real case scenario. Implications of mesh dependence are further discussed in chapter 4.

3.6 Parameter scaling

Accurate modeling of surface tension in multiphase flows can be challenging using the VoF method, due to material property discontinuities at the interface. In general it is found that inaccuracies in curvature computation lead to spurious currents [11]. In Gerris, the origins of spurious currents lie in computational accuracy of: curvature computation, advection scheme and surface tension scheme, as noted in [19]. In order to act against these unwanted artifacts, scaling of fluid properties can be executed using the similitude concept of paragraph 2.3.2. Reducing the material property discontinuities should reduce the spurious currents, and in particular, it is found that a reduction in density ratio is rather effective for simulations discussed in this work. Hence, the parameter rescaling procedure performed enforces a density ratio of $\rho_l/\rho_g = 5$, which automatically leads to a viscosity ratio of $\mu_l/\mu_g \approx \mathcal{O}(10)$.

Parameter scaling is also relevant for the maximum timestep used in Gerris. The software automatically determines an appropriate timestep based on the Courant-Friedrichs-Lewy (CFL) number and surface tension. The latter is important for inclusion of the shortest capillary waves present [19]. Hence a restriction is applied to the timestep, constraining the maximum timestep to be smaller for larger surface tension values. A consequence of high surface tension is therefore a high computational cost.

Chapter 4

Model validation

In this chapter, the software package Gerris is studied and validated for its ability to accurately simulate the different physics test cases described in Chapter 2. For simplicity and computational efficiency 2D cases are discussed. First the case of a static meniscus rising a vertical wall is discussed, followed by the dip coating case, a horizontal gas jet flow, and finally, the dip coating flow is combined with an impinging jet to study jet induced film thinning.

4.1 Meniscus rise

First, the correct implementation of the contact line angle and surface tension is validated using the case of a static meniscus rising at a vertical wall. Due to the restriction in density differences discussed in Chapter 3, all simulations use rescaled fluid properties while maintaining dynamical similarity. Both the physical and rescaled properties are shown in Table 4.1. The physical fluid properties are used for the remainder of this work. The gas phase contains the properties of carbon dioxide and the liquid phase represents water with the viscosity increased by a factor 10. This raise in viscosity increases dissipation of waves in the simulation and hence helps reduce the computational cost. The parameter file of the simulation leading to these results are shown in Appendix A.

Table 4.1: Physical and rescaled parameters of both the liquid and gas in dynamically similar systems. The liquid and gas parameters are distinguished by the subscripts l and g, respectively.

	Physical	Rescaled	Units
L	$2 \cdot 10^{-2}$	2	m
U_p	0.5	0.5	m/s
ρ_l	10^3	10	kg/m^3
ρ_g	2	2	kg/m^3
μ_l	10^{-2}	10^{-2}	kg/ms
μ_g	$1.5 \cdot 10^{-5}$	$1.5 \cdot 10^{-3}$	kg/ms
γ	$7.2 \cdot 10^{-2}$	$7.2 \cdot 10^{-2}$	kg/s^2
g	9.81	$9.81 \cdot 10^{-2}$	m/s^2
θ_E	60	60	degrees
t	10^{-2}	1	s

The simulation is set up in a square box with at the bottom a liquid reservoir and atop the gas phase, as shown in Figure 4.1a. The box size has been set to be sufficiently large at several times the capillary length, namely $L > 7l_c$. A no-slip boundary condition is implied on the left wall with a fixed equilibrium contact line angle of $\theta_E = 60°$. The right hand side and bottom wall are free slip walls. The top is an open boundary maintaining a pressure of $p = 0$ Pa.

Starting a simulation from an initially flat interface such as depicted in Figure 4.1a causes waves which persist for long periods of time, $t > 200$ s (rescaled quantity). To reduce the influence of surface waves, the simulation is restarted with a meniscus initialized[1] to the height found in the simulation perturbed by waves. This new initialized interface is denoted by the dotted line in Figure 4.1a. The simulation containing the initialized meniscus interface also produces waves. However, employing this procedure reduces the amplitude of waves present, thus allowing it to be resolved faster by viscous dissipation.

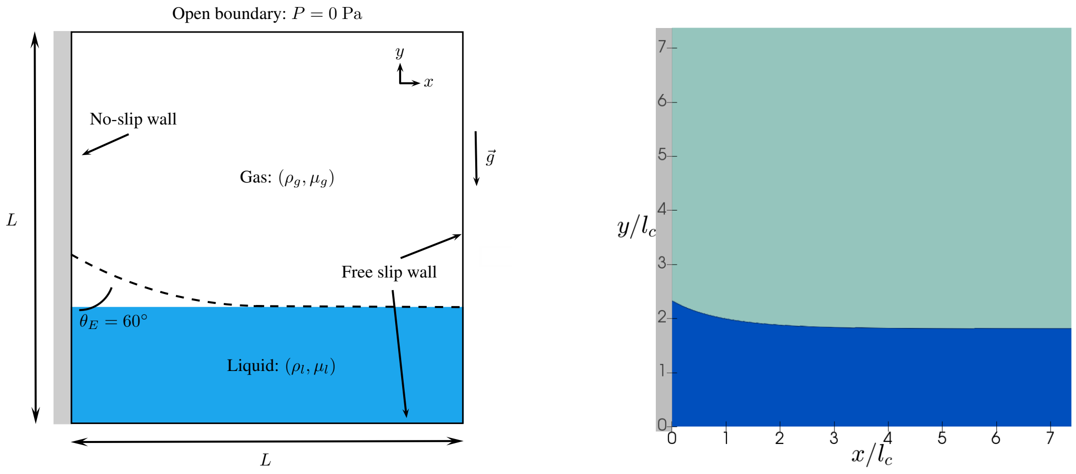

(a)

(b)

Figure 4.1: a) Schematic representation of the initial conditions of the static meniscus test case. In blue the initial interface of the first simulation is shown. The dotted line resembles the meniscus at a height resulting from this simulation. This height was then used to approximate a meniscus shape of the initial liquid-gas interface for the second simulation. b) Stationary solution of the simulation at $t = 200$ s (rescaled quantity), revealing the capillary rise at the left side of the domain on a vertical wall. In blue a fluid with the properties of water is shown, with the exception of viscosity, being ten times the normal value. Teal indicates the gas phase possessing the properties of carbondioxide.

The stationary solution of the simulation started with an initial meniscus is achieved after $t = 200$ s (rescaled quantity) and is shown in Figure 4.1b. Extraction of the liquid-gas interface from Figure 4.1b allows for comparison with the analytical solution of equation (2.39), as presented in Figure 4.2. As shown, the simulation result matches the analytical solution.

---

[1] Using an exponential function with empirically found parameters

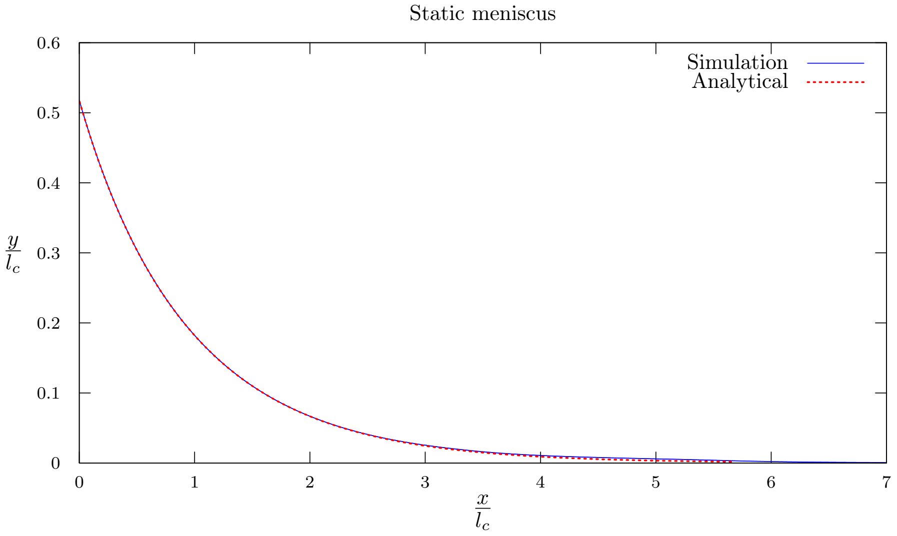

Figure 4.2: Comparison of simulation results with the analytical solution. The interface between the liquid and gas phase extracted from Figure 4.1b is indicated by the blue line. The dotted red line indicates the analytical solution of the capillary rise at a vertical wall determined by equation (2.24). Note that the vertical axis is shifted compared to Figure 4.1b, such that $y/l_c = 0$ now refers to the liquid-gas interface on the right hand side of the domain.

4.2 Dip coating flow

The next step is to validate the physics of a dynamic case by simulating the entrainment of a dip coating film. The velocity of the plate is chosen to be $\text{Ca} > \text{Ca}_{\text{cr}}$, such that film entrainment is observed. The simulation is made out of one box in Gerris with a box size of $L \approx 30l_c$. The setup of boundary conditions is similar to the case of the static meniscus rise. A schematic representation of the dip coating simulation is shown in Figure 4.3a. On the left hand side, a no-slip wall moving upward (in positive y-direction) with a velocity $U_p = 0.5$ m/s, and an equilibrium angle $\theta_E = 60°$. The bottom and right hand side walls are free slip walls to constrain the fluids. The top boundary is an open boundary set to a static pressure of zero. The simulation is run for $t = 25$ s (rescaled quantity), at which point the contact line has surpassed the top boundary. The initial setup starts with a liquid reservoir at the bottom of the domain at a height of approximately $1/10^{\text{th}}$ of the domain size. Above the liquid a gas is present up to the top boundary. The physical and rescaled fluid properties are shown in Table 4.2. Additional details for this simulation are shown in the parameter file set reported in Appendix B.

A snapshot at $t = 22$s (rescaled value) of the simulation can be seen in Figure 4.3b with an additional close-up of the film shown in Appendix C. The result clearly shows film pulling with build-up of fluid near the front of the film. A time-lapse of the interface between phases can be seen in Figure 4.4. Here the final result clearly shows the ridge build-up and the capillary shock.

4.2.1 Landau-Levich film

The liquid-gas interface of the Landau-Levich film can be extracted from the simulation at $t = 22$ s (rescaled quantity), shown up to the capillary shock in Figure 4.5. Here the dotted line denotes the Landau-Levich film thickness solution of equation (2.33). Note that the theoretical solution is obtained by asymptotical matching, and the simulated film thickness is therefore only supposed to approach the solution. Figure 4.5b shows the vertical velocity profile through horizontal planes at various heights. Revealing the flow profiles from the wall, $x/l_c = 0$, up to the local film thickness.

Furthermore, visual inspection of the time lapse in Figure 4.4 reveals that the Landau-Levich

Table 4.2: Physical and rescaled parameters of both the liquid and gas in dynamically similar systems. The liquid and gas parameters are distinguished by the subscripts l and g, respectively.

	Physical	Rescaled	Units
L	$8 \cdot 10^{-2}$	8	m
U_p	0.5	0.5	m/s
ρ_l	10^3	10	kg/m^3
ρ_g	2	2	kg/m^3
μ_l	10^{-2}	10^{-2}	kg/ms
μ_g	$1.5 \cdot 10^{-5}$	$1.5 \cdot 10^{-3}$	kg/ms
γ	$7.2 \cdot 10^{-2}$	$7.2 \cdot 10^{-2}$	kg/s^2
g	9.81	$9.81 \cdot 10^{-2}$	m/s^2
θ_E	60	60	degrees
t	10^{-2}	1	s

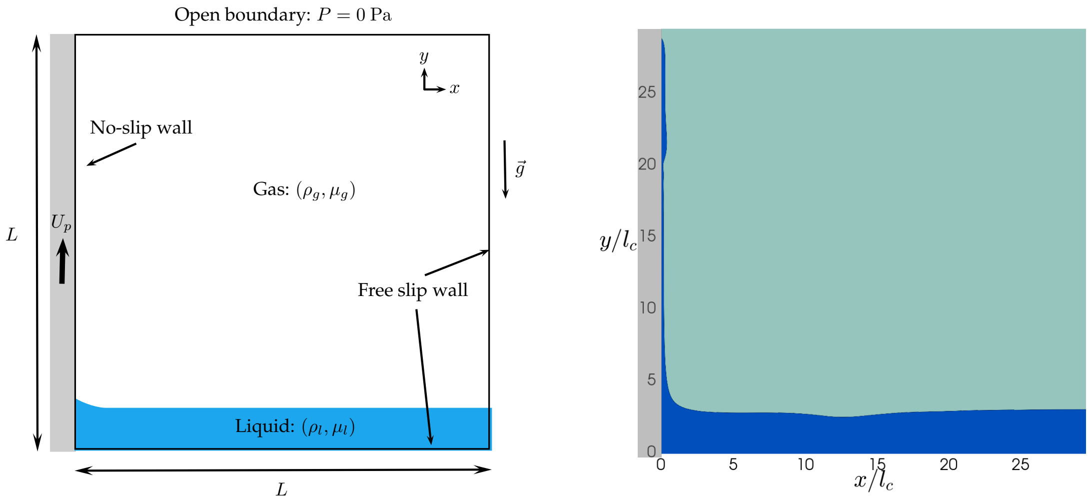

(a) (b)

Figure 4.3: a) Schematic representation of the dip coating simulation. The wall on the left hand side is now a moving wall with a velocity U_p. The top boundary is again a open boundary, and the bottom and right hand side again employ a free slip boundary condition. b) Density plot of the results obtained at $t = 22$ s (rescaled quantity). In blue the liquid phase is shown, and in teal the gas phase.

film does not immediately acquire a fixed thickness. Hence the film thickness is recorded over time at a fixed vertical position of $y/l_c = 10$ shown in Figure 4.6. The graphs show that after the ridge front passes, the film does not immediately adopt a fixed film thickness, instead, the film thickness increases in time.

4.2.2 Film ridge

Also the front ridge can be isolated from the capillary shock up to the contact line, as shown in Figure 4.7a. Here the dotted line resembles the solution of equation (2.35), estimated using the resulting U_{cl} of the simulation. The value is expected to hold close to the contact line around $y/l_c \approx 27$. The capillary shock clearly shows resemblance to the experimental work of [21]. Figure 4.7b shows the vertical velocity profile near the thickest part before the transition zone, the thin middle section, and the liquid front.

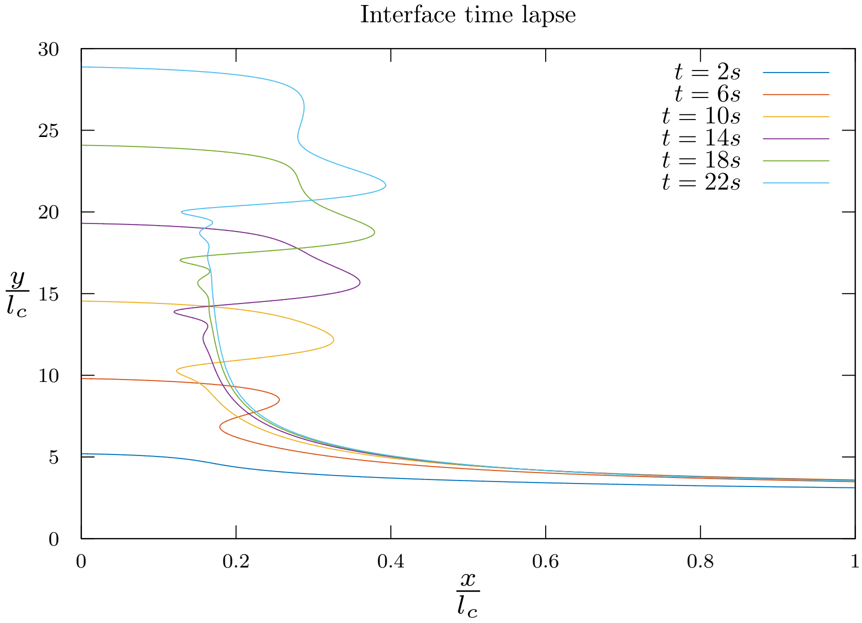

Figure 4.4: Time lapse of the interface profile, the horizontal scale has been stretched such that the relevant phenomena are visible. The time step in the legend denote rescaled quantities.

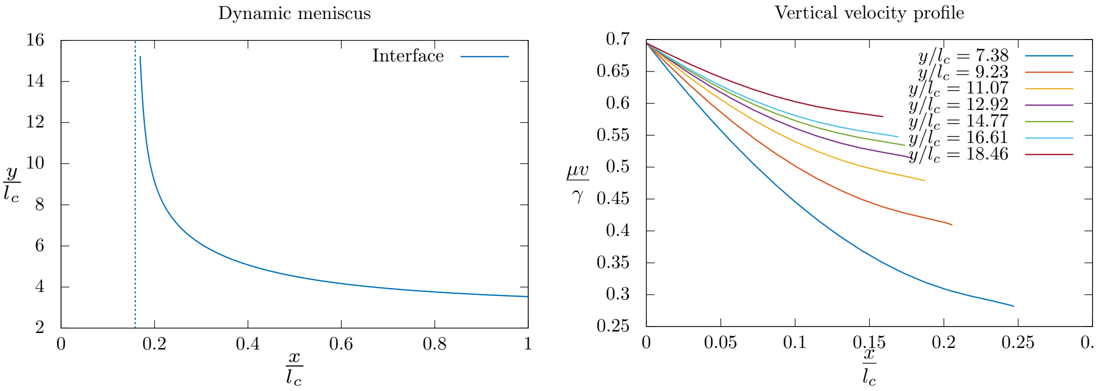

(a) (b)

Figure 4.5: a) Lower half of the dip coating film up to the capillary shock. Again the horizontal axis is stretched. The dotted line indicates the solution according to the Landau-Levich equation (2.33): $x/l_c = 0.159$. b) Shows the vertical velocity profile, v, through horizontal planes positioned at various heights. Note that the velocity increases as the film becomes thinner due to mass conservation.

4.2.3 Mesh dependence

As described in paragraph 3.5.2 the Cox-Voinov model requires a molecular length scale to approximate the behavior of the contact line. The value of this length scale is material dependent and unknown prior to the simulation. Therefore, Gerris approximates this value using a fraction of the mesh size. As a result, the velocity of the contact line is dependent on the mesh size. An example can be seen in Figure 4.8, where a decrease in the mesh size by a factor 2 reveals an approximate 15% reduction in vertical distance traveled by the contact line with respect to the

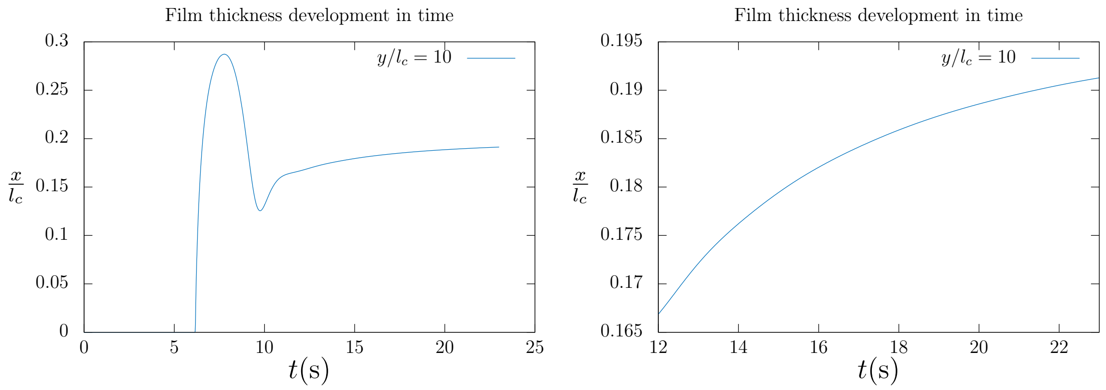

(a)

(b)

Figure 4.6: a) Film thickness at a fixed vertical position of $y/l_c = 10$ over time. Clearly visible is the film front ridge and the capillary shock b) Close-up of the film development after the capillary shock.

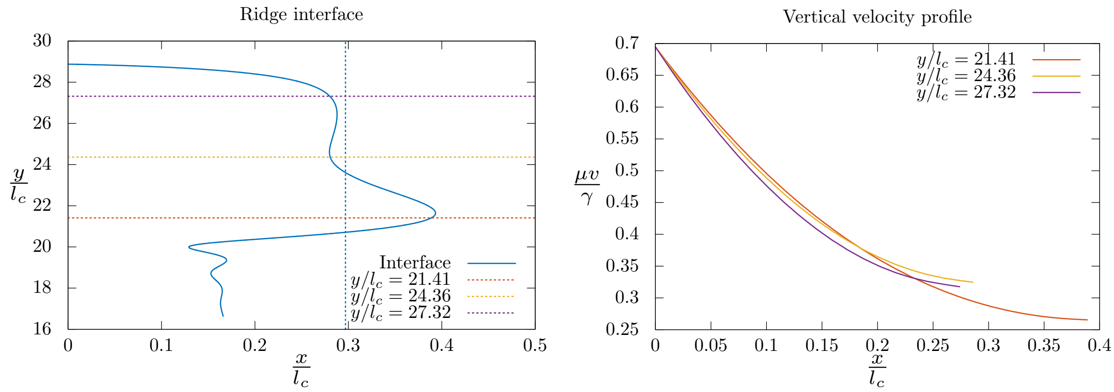

(a)

(b)

Figure 4.7: a) Interface of the ridge including the transition zone to the Landau-Levich film. The vertical dotted line resembles the theoretical solution for the ridge film thickness close to the contact line given by equation (2.35) using U_{cl} from the simulation, leading to an expected ridge thickness of $e_r/l_c = 0.297$. The horizontal lines denote the heights at which the velocity profiles reported in panel b) are obtained. b) Vertical velocity profile through a thick section of the jump, a thin middle section and the film front.

reservoir.

The accurate setup of a physical case therefore requires a correction to the microscopic length scale. This can be accomplished by choosing the domain and mesh such that the contact line velocity of the simulation matches the physical case. In order to determine the mesh dependency, a simulation setup can be solved for different mesh sizes. From these simulations, the contact line velocity can be measured and compared with one another. However, because the slip velocity relative to the plate does not change, i.e. the relative capillary number (Ca*) is constant, a more accurate approach is to include additional measurements obtained from different wall velocities. This method results in an average constant value of Ca* for each of the refinement levels, as reported in Figure 4.9.

The data is gathered by tracking the velocity of the interface a few cell sizes apart from the moving wall, and averaging the outcome over time. As it turns out, inaccuracies caused by this method do not allow to distinguish the mesh refinement dependence, albeit it does show that the relative capillary number is indeed independent of the plate velocity (due to the horizontal red line in Figure 4.9).

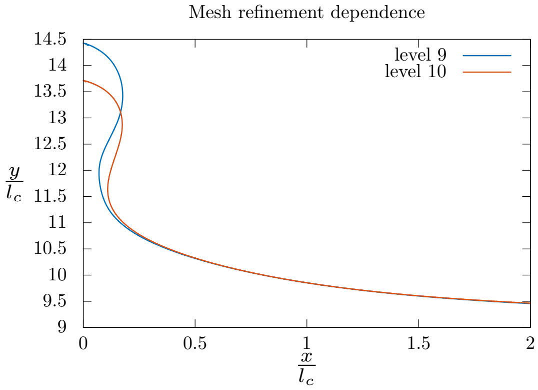

Figure 4.8: Entrained film progression for different levels of refinement with $\mathrm{Ca} = 1.39 \cdot 10^{-2}$. A refinement level indicates the amount of cells every direction of a domain is divided into. A refinement level of 9 corresponds to 2^9 cells in one direction of the domain. The interfaces are extracted at the same time $t = 1.5$s.

4.2.4 Equilibrium angle dependence

In addition to the mesh dependence, inaccuracies of the contact line angle can also result in contact line velocities different than expected. In order to quantify this, various θ_E are simulated and the results are reported in Figure 4.10. As indicated by the linear fit, a deviation could lead to a velocity increase of approximately 1.5% per degree for this particular case.

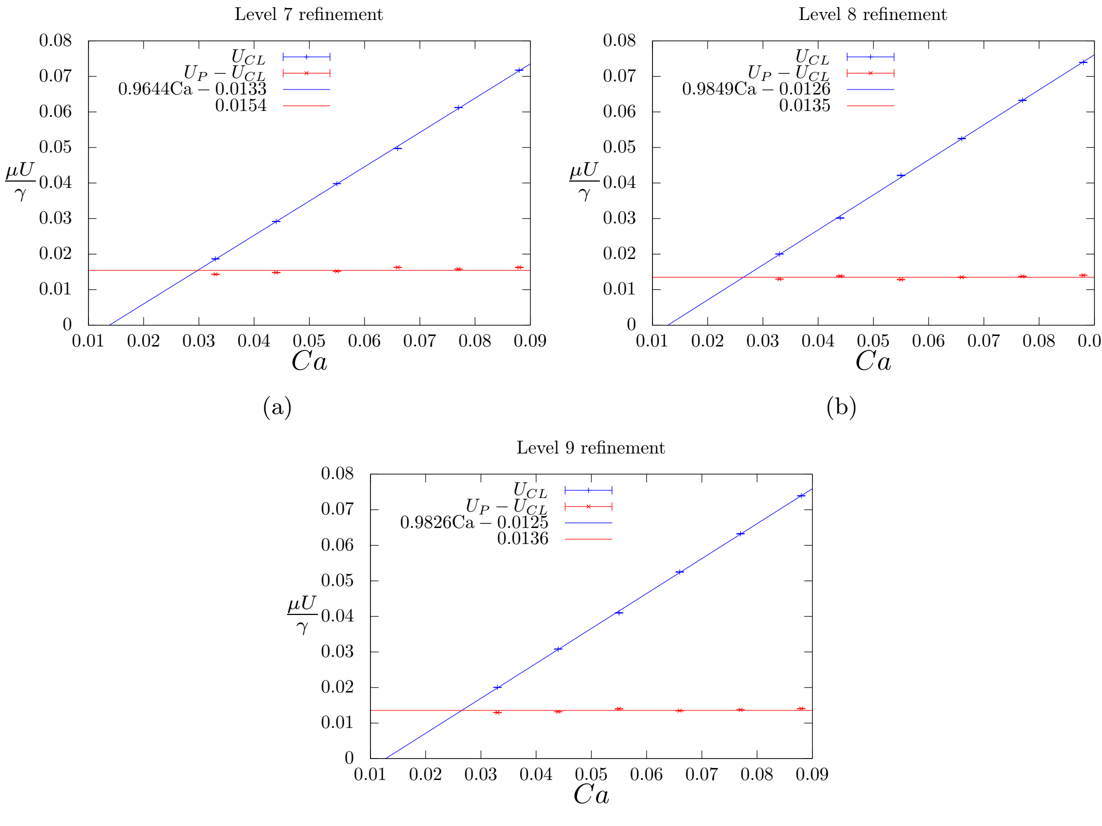

(a) (b)

(c)

Figure 4.9: (a)(b)(c) Mesh dependence of different mesh refinement levels: 7,8, and 9, respectively (i.e. the domain is split into: $2^7 \times 2^7$, $2^8 \times 2^8$, and $2^9 \times 2^9$ mesh boxes, respectively). The horizontal axis shows the wall velocity in dimensionless units, the vertical axis indicates the dimensionless velocities of the contact line (U_{cl}) and the relative difference between contact line and wall $U_p - U_{cl}$ (Ca^*) in blue and red, respectively.

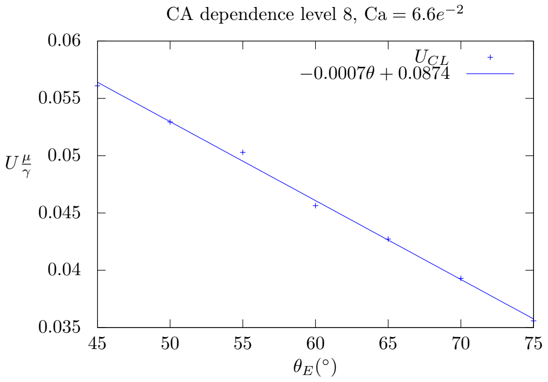

Figure 4.10: Contact line velocity dependence on the equilibrium contact angle, θ_E.

4.3 Jet flow

The third case is that of a jet flow. The jet behaviour is visualized before implementing it in the dip coating simulation. For this model, a domain of equal size as the dip coating simulation is used. A schematic representation of the domain with a detailed description is displayed in Figure 4.11. Here, the boundary on the left hand side is a rigid no-slip wall, while the bottom, right hand side, and top boundary are open, with a constant hydrostatic pressure, $p = \rho_g g(L - y)$ (the origin is at the bottom left of the domain). A horizontal jet, with a nozzle width of $L_j/l_c = 0.69$, is implemented at a central height, $L_y/l_c = 13.15$. This jet reaches from the open boundary on the right up to a distance of $x/l_c = 3.00$ away of the left wall. Details of the domain and of the gas used in the domain are reported in Table 4.3, with U_j the jet velocity setpoint used in the simulation.

Table 4.3: Physical and rescaled parameters for both the liquid and for the gas in dynamically similar systems.

	Physical	Rescaled	Units
L	$8 \cdot 10^{-2}$	8	m
U_p	0	0	m/s
U_j	2	2	m/s
ρ_g	2	2	kg/m^3
μ_g	$1.5 \cdot 10^{-5}$	$1.5 \cdot 10^{-3}$	kg/ms
g	9.81	$9.81 \cdot 10^{-2}$	m/s^2
t	10^{-2}	1	s

Gerris only allows to set one boundary condition per boundary. Hence it is not possible to have both an inlet velocity boundary and a open boundary condition on the right hand side. Therefore the jet flow is generated using a local body force with an accelation of $\vec{a} = (a_x, 0)$, applied on the fluid in the teal region of Figure 4.11. The acceleration function is based on a proportional control function used in control systems. In this case, the function regulates to a desired jet velocity U_j. The accelerating control function is tuned in order to force a parabolic flow profile:

$$a_x(y, u) = \left[1 - \frac{4(y - L_y)^2}{L_j^2}\right](u - U_j) \tag{4.1}$$

Where L_y is the center height and L_j the jet width, shown in Figure 4.11. The proportional control function is applied in the teal region only, i.e. $(L_y - \frac{1}{2}L_j) < y < (L_y + \frac{1}{2}L_j)$. Notice that at the nozzle walls the acceleration is $a_x(y = L_y \pm \frac{1}{2}L_j, u) = 0$, it is velocity dependent in the center of the jet $a_x(y = L_y, u) = u - U_j$ and it vanishes when the velocity is equal to the setpoint value $a_x(y, u = U_j) = 0$.

The acceleration control function is only applied in the teal region of the nozzle to allow the flow to fully develop. It is empirically found that a different flow profile of, for instance, a flat acceleration profile ($a_x(u) = u - Uj$) does not influence the flow profile at the nozzle opening.

A disadvantage of using a proportional control function is that it produces a steady state error that may be eliminated by using a more complex control function. In this case, however, the error does not pose a problem since the steady jet velocity value can be obtained from simulation data at the nozzle centerline.

The result of the simulation are displayed in Figure 4.12. Figure 4.12a shows a snapshot of the simulation after $t = 6$ s (scaled quantity), revealing a steady jet flow. After some time, the flow starts to oscillate in upward and downward direction. This oscillatory movement is shown in Figure 4.12b after $t = 16.5$ s (scaled quantity).

Additionally, simulation results can be used to validate the jet velocity control function. Figure 4.13a shows the velocity profile through the nozzle exit, $x/l_c = 3.00$. The result reveals a Poiseuille flow profile as expected. Furthermore, the volumetric flow rate is displayed in Figure 4.13b, showing that the jet reaches a constant flow rate within $t = 5$ s (scaled quantity), maintained until the end of the simulation. With the flow profile and volumetric flow rate of the jet validated, it can now be applied in a dip coating simulation to investigate film thinning.

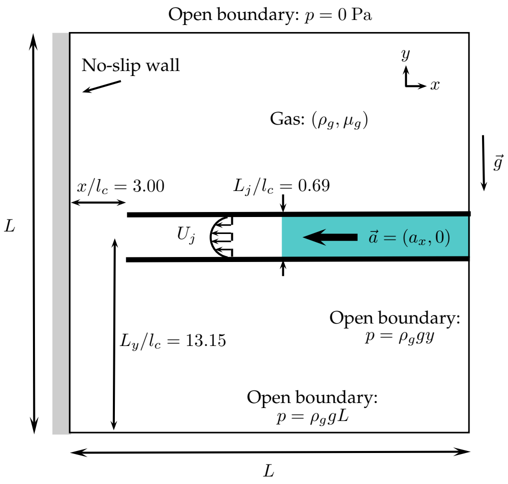

Figure 4.11: Schematic representation of the jet simulation setup. On the left hands side is a no-slip wall, while the bottom, the right and the top boundary conditions are set to open boundaries with a fixed pressure of $p = \rho_g g(L - y)$. The gas is accelerated in the teal region using the proportional control function denoted by $\vec{a}$.

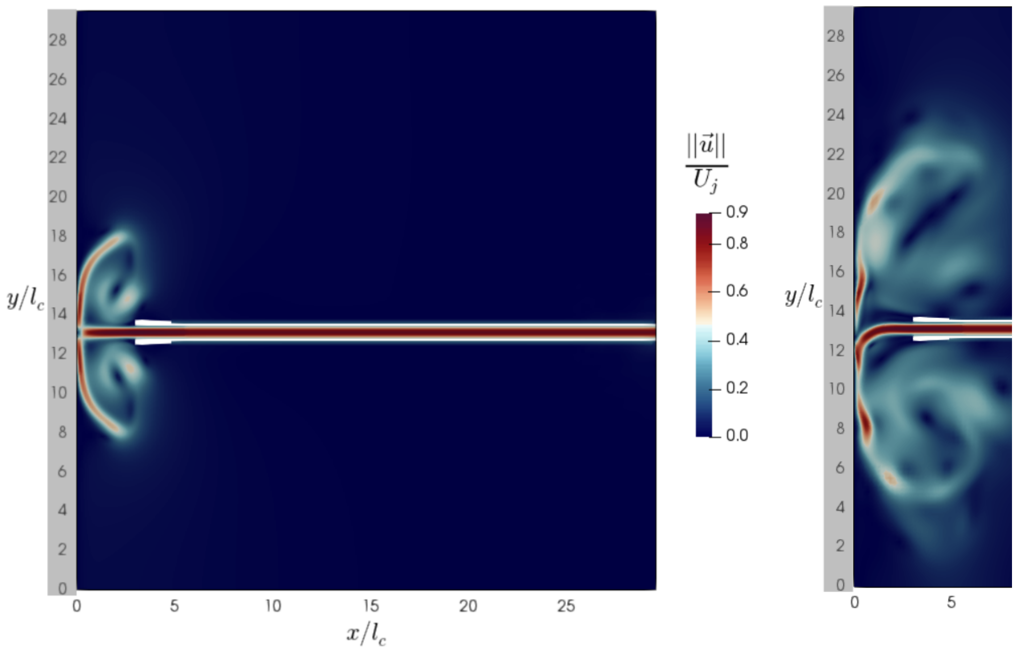

(a)

(b)

Figure 4.12: a) Jet behaviour at $t = 6$ s (scaled quantity). The velocity is shown relative to the velocity setpoint $U_j = 2$ m/s. b) A close-up of the left part of the domain after several up- and downward oscillating motions at $t = 16.5$s (scaled quantity).

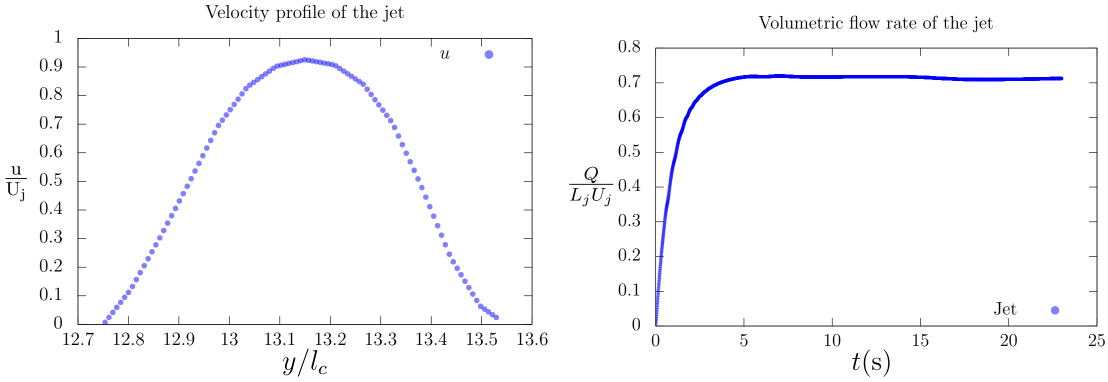

(a) (b)

Figure 4.13: a) Jet flow profile at $t = 22$ s (scaled quantity). b) Volumetric flow rate through the nozzle exit $x/l_c = 3.00$. Differences between the data points and the average after $t = 5$ s result in a variance of $\sigma^2 = 1.36 \cdot 10^{-6}$.

4.4 Dip coating film impinged by a jet

The dip coating and jet models are now combined to investigate the influence of a jet on a dip coating film. For this model, the domain is of equal length compared to the dip coating and jet simulations. A schematic representation of the domain with a detailed description is displayed in Figure 4.14. The dimensions of the jet nozzle are the same as shown in Figure 4.11. On the left hand side the moving wall is shown, moving at a velocity U_p. The boundaries on the top and on the right are open boundaries, again set to a hydrostatic pressure, $p = \rho_g g(L - y)$. Free slip boundary conditions are used for the bottom and reservoir wall.

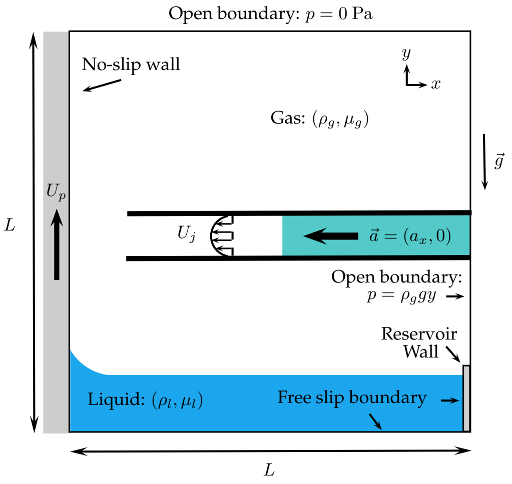

Figure 4.14: In blue the liquid reservoir is shown with a meniscus shape at the start of the simulation. The rest of the domain is filled with gas, with in teal the region where the proportional function $\vec{a}$ is active. In addition to previous simulations, a reservoir wall is implemented in the bottom right corner of the domain to retain the fluid in the reservoir. A free slip boundary condition is imposed on both the reservoir and on the bottom wall.

For the domain displayed in Figure 4.14, multiple simulations are performed in a parameter sweep, to investigate film thinning by the jet. The parameters varied are the jet velocity setpoint U_j and wall velocity U_p, as these quantities determine $\mathrm{Re_j}$ and Ca of equation (2.39), respectively. Fluid properties and velocity ranges used are reported in Table 4.4.

Table 4.4: Physical and rescaled parameters of both the liquid and of the gas in dynamically similar systems. The liquid and gas parameters are distinguished by the subscripts l and g, respectively. The parameters U_p and U_j contain a range of values used in the parameter sweep.

	Physical	Recaled	Units
L	$8 \cdot 10^{-2}$	8	m
U_p	$0.7 - 1.5$	$0.7 - 1.5$	m/s
U_j	$1.5 - 5.0$	$1.5 - 5.0$	m/s
ρ_l	10^3	10	kg/m^3
ρ_g	2	2	kg/m^3
μ_l	10^{-2}	10^{-2}	kg/ms
μ_g	$1.5 \cdot 10^{-5}$	$1.5 \cdot 10^{-3}$	kg/ms
γ	$7.2 \cdot 10^{-2}$	$7.2 \cdot 10^{-2}$	kg/s^2
g	9.81	$9.81 \cdot 10^{-2}$	m/s^2
θ_E	60	60	degrees
t	10^{-2}	1	s

An example of film thinning is shown in Figure 4.15. In this particular setup, the wall velocity is, $U_p = 1.0$m/s or Ca $= 13.9 \cdot 10^{-2}$ and the jet velocity setpoint $U_j = 2$ m/s resulting in $\mathrm{Re_j} = 69.5$. The result clearly shows film thinning after the jet and fluid build-up before the jet. The dynamic shape of fluid build-up causes wave formation in the film after the jet. These waves stabilize once a static shape is formed such as shown in Figure 4.15. For high jet velocities, shear stress applied by the jet is sufficient to tear apart the fluid build-up, resulting in an inaccurate droplet separation since both radii, R_1 and R_2, of the Laplace equation (2.8) are required for this phenomenon, i.e. a 3D model is required for accurate droplet separation computations.

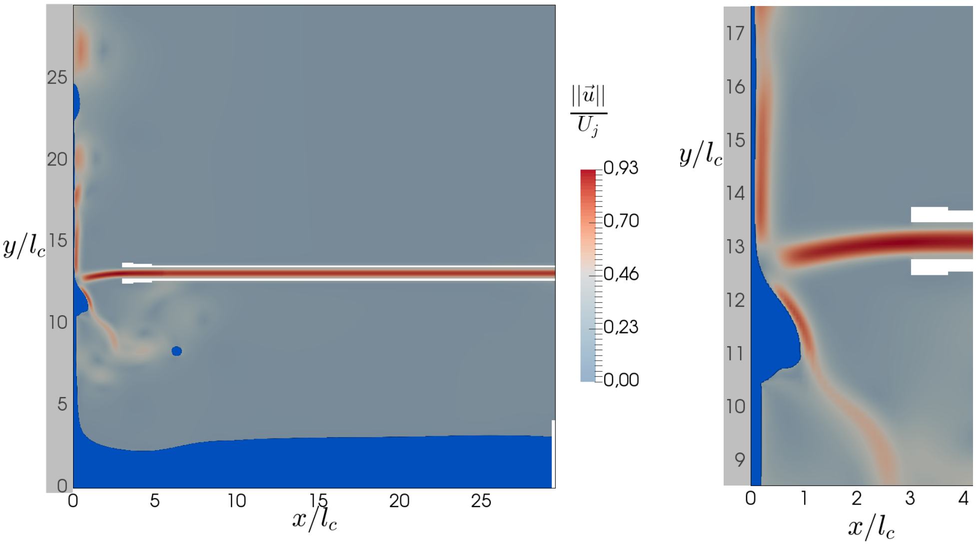

(a)

(b)

Figure 4.15: a) Progression of an impinged film at $t = 10$ s with, in blue, the liquid and, in grey to red colorscale, the velocity profile of the gas phase. The jet velocity setpoint is $U_j = 2$ m/s (scaled quantity). The relevant dimensionless numbers are $\mathrm{Re_j} = 68.7$ and Ca $= 13.9 \cdot 10^{-2}$ b) Close-up of the jet impact region, clearly showing film thinning and fluid build-up.

4.4.1 Jet velocity dependence

A parameter sweep on jet velocities allows to relate the jet velocity to the film thickness. This procedure is performed in a relatively small range of jet velocities (as reported in Table 4.4) and shown in Figure 4.16 for a constant wall velocity, $U_p = 1$ m/s, corresponding to Ca $= 13.9 \cdot 10^{-2}$. Data in blue covers the film thinning due to the jet, with horizontal inaccuracies due to the proportional velocity control function of the jet and vertically due to waves in the film. A fit function is obtained by a linear fit in logarithmic scale, reported in Figure 4.16b, resulting in a film thickness dependence of:

$$e_j = f(\mathrm{Ca}, \mathrm{Ca}^*, l_c)\mathrm{Re_j}^{-2.41} \tag{4.2}$$

which applies to films capable of advancing past the jet. The latter point must be emphasized, since the jet can influence the liquid front shape to such a point that entrainment could possibly be inhibited by an increased contact line velocity relative to the plate.

Additionally the graph shows, in red, the film thickness prior to the jet at $y/l_c = 10$. For low jet velocities no significant differences are observed. For high jet velocities, however, the shear stress of the jet flow leads to waves in the film prior to the jet ($y/l_c < 10$). These waves perturb the meniscus, leading to an overall thinner film prior to the jet.

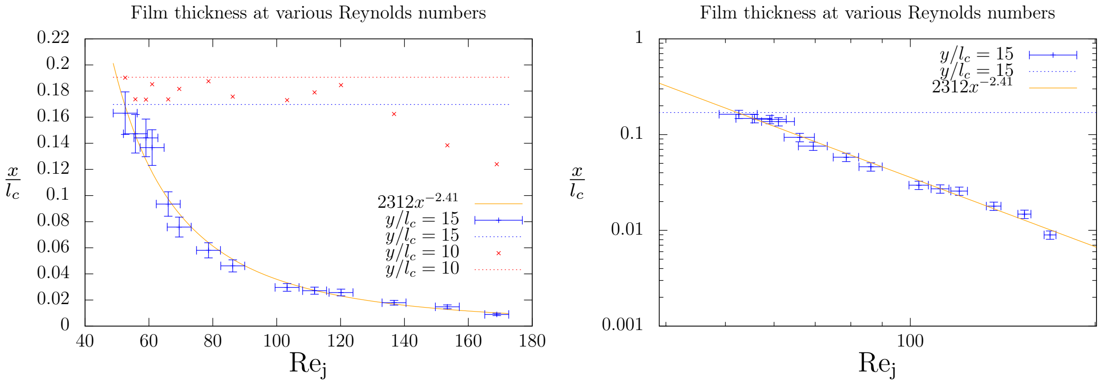

(a)

(b)

Figure 4.16: a) Film thickness before (red) and after (blue) the nozzle for various jet Reynolds numbers. The dotted lines denote the film thickness without the implementation of the jet. The error bars indicate three times the standard deviation of the measured dispersion. b) Log-log plot of the same data of panel a) including the fitting function.

Film thinning does not necessarily mean a reduced volumetric flow rate, due to possible speed up of the film flow. To quantify this, volumetric flow rate is measured at a fixed vertical position of $y/l_c = 15$. An example is shown in Figure 4.17b obtained from the simulation reported in Figure 4.15 (Figure 4.17a shows the control measurement without a jet). The control measurement graph is similar to Figure 4.6, due to $v(x, y = 15l_c) \approx U_p$ as shown in Figure 4.5b (which uses a lower wall velocity). The volumetric flow rate in the thinned film Figure 4.17b shows a significant influence of wave formation in both the ridge and thinned film. The graphs are reproduced for the majority of jet Reynolds numbers used and shown in Appendix G Figure G.1. The average volumetric flow rate, Q, in the thin film parts of these simulations are extracted and shown in Figure 4.18, again revealing a decline for increasing jet velocities, scaling as $Q \propto \text{Re}^{-2.26}$.

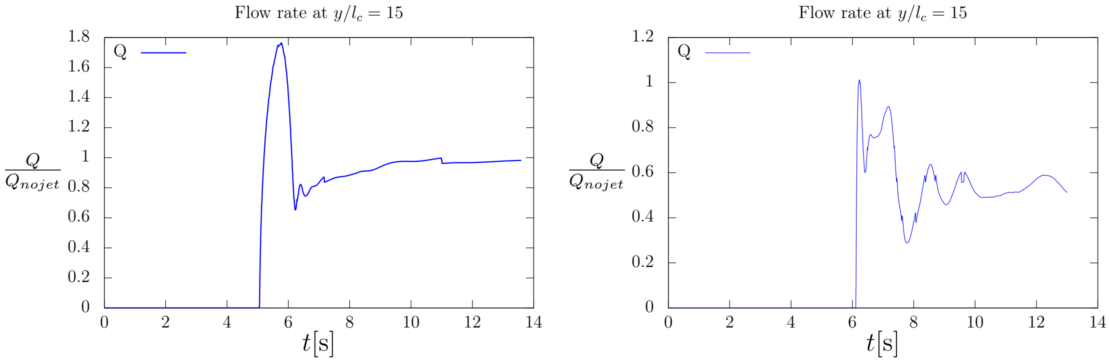

(a)

(b)

Figure 4.17: a) Flow rate of a dip coating film, without a jet and for $\text{Ca} = 13.9 \cdot 10^{-2}$, normalized by the volumetric flow rate $Q_{nojet} = 4.31 \cdot 10^{-2}\text{m}^2/\text{s}$ (scaled units) in the Landau-Levich film measured at $y/l_c = 15$. b) Flow rate of the simulation shown in Figure 4.15, again normalized by Q_{nojet}.

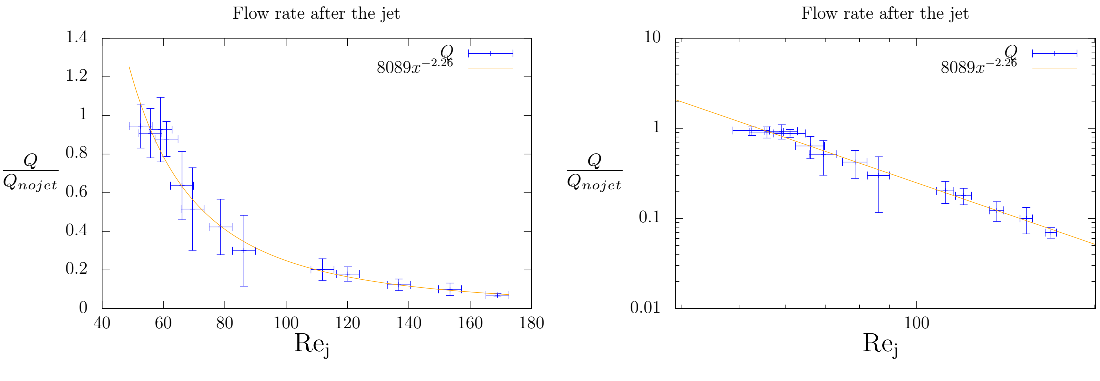

(a) (b)

Figure 4.18: a) Flow rate for various jet Reynolds numbers normalized by Q_{nojet}. The reported error bars is estimated as three times the standard deviation. b) Logarithmic plot of the data including the fit funciton.

4.4.2 Wall velocity dependence

Similar to the jet velocity dependence, the wall velocity can be varied to study its influence, as shown in Figure 4.19 for a fixed $\mathrm{Re_j} = 68.7$. The blue measurements indicate that the film thickness indeed increases with the wall velocity. However, a decreasing trend in the thickness of the measurements prior to the jet in red is observed, while equation (2.36) predicts an increasing trend with the capillary number. The cause for this trend is the time at which the measurements are taken, as faster moving films reach the top domain boundary sooner, hence, forcing the thickness measurements to be taken earlier in time, which, according to Figure 4.6 leads to a misinterpretation of the film thickness. Nevertheless, the film thickness is found to increase after the jet for higher wall velocities, even though the method employed does not allow for a proper quantitative description due to the misinterpretation of the film thicknesses.

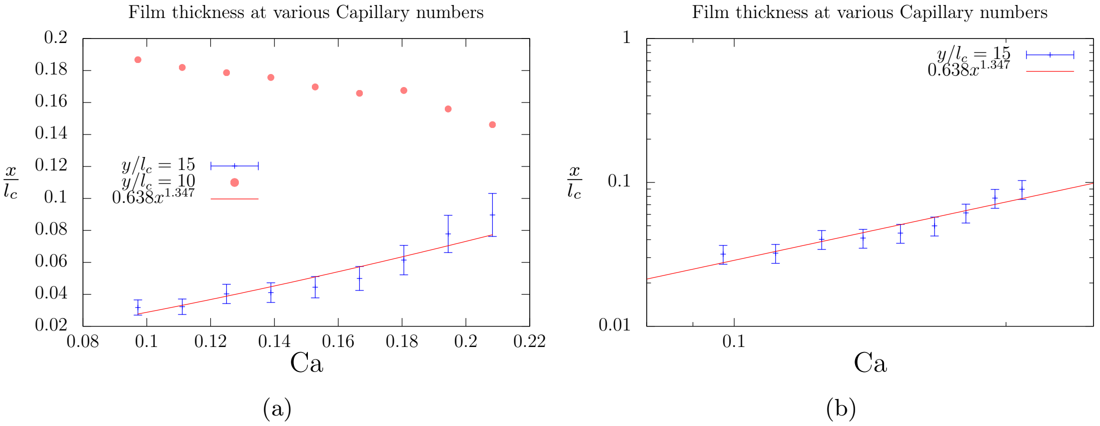

(a) (b)

Figure 4.19: a) Film thickness before (red) and after (blue) the nozzle for varies wall velocities. b) Log-log plot of the data including the fitting function.

4.4.3 Contact line velocity

The contact line velocity associated with the simulation of Figure 4.15, is reported in Figure 4.20, revealing a difference in the contact line velocity moving towards and away from the jet. More specifically, the figure shows a significant decrease in velocity when approaching the jet and a significant increase in surpassing the jet impact zone. Additional plots for different configurations are shown in Appendix F, namely Figure F.1 and Figure F.2.

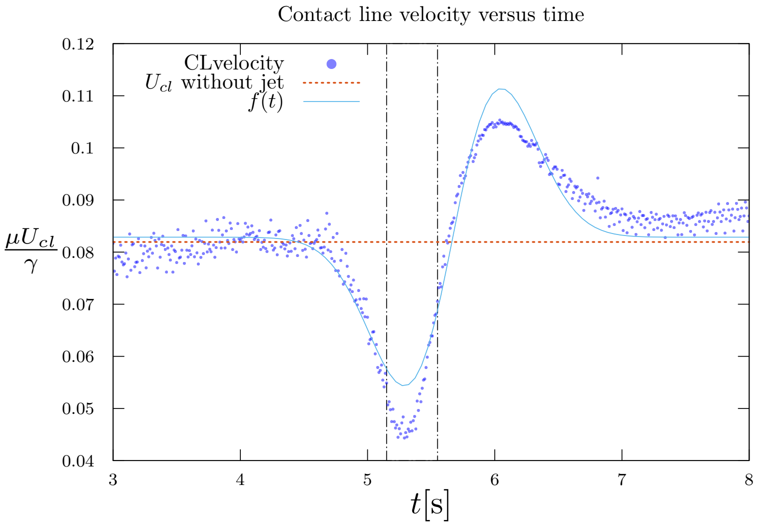

Figure 4.20: Contact line velocity versus time for the simulation shown in Figure 4.15. The vertical lines indicate when the contact line passes the nozzle walls, at $\mathrm{Re_j} \approx 69$ and $\mathrm{Ca} = 13.9 \cdot 10^{-2}$. Note that jet bending is not taken into account. The fitting function is chosen as the derivative of a Gaussian function, $f(t) = a(x-c)exp[-b(x-c)] + d$, with fitting parameters reported in Table F.1.

Specific configurations of the model reveal a stagnant contact line at the jet impact region. The immobility of the contact line is however accompanied by a high curvature at the contact line, requiring a finer mesh size for accurate simulations. In turn, a different mesh size will result in different contact line dynamics due to its mesh dependence, i.e. different slip velocity, such that it is not possible to have both accurate simulations of contact line retention and be able to compare the simulation results with those included in this report.

Chapter 5

Conclusions

In this work, numerical studies are presented related to the classical Landau-Levich flow problem using the open source software Gerris. All investigations were performed in 2D due to the higher computational cost of fully 3D simulations, and also due to the high level of mesh refinement required for accurate modelling of the liquid-gas interface and contact line dynamics. The case studies represent dynamically similar systems of a viscous fluid in contact with a vertical wall.

The first case studied is that of a meniscus rising due to wetting at a vertical solid wall. Both the height and contact line angle comply with the theoretical predictions, and the shape of the liquid-gas interface converges to the analytical solution. The results of this case study thereby helps to validate the proper implementation of the physics involved: surface tension, wetting, and the numerical discretization of the interface.

The second case studied is the dip coating setup. The dynamical development of the entrained film on the wall as it is withdrawn from the liquid reservoir, reveals a ridge at the film front, followed by the Landau-Levich film. The Landau-Levich film approaches the thickness predicted by Landau and Levich, whereas the front ridge agrees with the thickness predicted, using the contact line velocity from the simulation. Both the film front and the Landau-Levich film reveal a Poiseuille flow profile. In the Landau-Levich film it is found that the flow profile speeds up as the film becomes thinner. This acceleration is caused by mass conservation, as the film thins to the thickness predicted by Landau and Levich. Also observed in the simulations is the capillary shock in the transition between the front ridge and the Landau-Levich film, being of similar shape as in the work of [21]. Furthermore, it is shown that the slip velocity between the wall and the contact line is constant, regardless of the wall velocity. Hence, it is known that the ridge thickness and the slip velocity can only be dependent on the equilibrium contact line angle.

In the numerical results however, the model for the contact line dynamics is mesh dependent, as Gerris uses quantities determined by the mesh size. This, in turn, makes also the slip velocity mesh dependent (in addition to the equilibrium angle dependence). Even though a mesh dependence is clearly observed, no quantitative description for it could be obtained. Therefore, it can be concluded that Gerris is capable of accurately simulating dip-coating problems, once it is accepted that the contact line velocity and front ridge thickness are mesh dependent (this might lead to some level of inaccuracies in the front ridge).

The third case studied discussed is that of a laminar jet setup. The jet flow used in this work is in the laminar regime ranging from $\mathrm{Re_j} \approx \mathcal{O}(10^1) - \mathcal{O}(10^2)$. In order to generate the jet, a proportional control function is employed to regulate the jet velocity by applying a body force on the gas in the jet nozzle. It is found that the jet flow profile at the nozzle exit is a Poiseuille flow profile. The results also show that the jet volumetric flow rate stabilizes to a constant value, proving that the proportional controller is stable in this system. It is found that vorticity is generated at the start of the simulation, perturbing the jet flow and causing an up- and downward oscillatory motion of the jet flow. The oscillatory motion is however not observed when the jet is applied to a dip coating film. From the results of the simulation, it can be concluded that a local body force controlled by a proportional control function allows to generate a jet flow that regulates to a constant velocity. A specified jet velocity can be accurately obtained, if the steady state error in the proportional control function is taken into account.

Finally, in the fourth case studied, dip coating and jet are combined to investigate the novel phenomenology that emerges due to jet film thinning. In particular the influence of the jet and of the wall velocities are investigated. From the simulations performed, film thinning is observed at the jet impact zone, where the fluid tends to accumulate. The fluid accumulation gives rise to a second ridge just below the jet impact zone, pinning the jet flow on top.

The dependence of the film thinning on the jet velocity is performed by a parameter sweep, using a small range of jet velocities in the order of $\mathrm{Re_j} \approx \mathcal{O}(10^1) - \mathcal{O}(10^2)$. A relation between the film thickness, e_r, and the jet Reynolds number is found to be $e_j \propto \mathrm{Re_j}^{-2.41}$, which is only valid for films that pass the jet. Furthermore, it is found that the volumetric flow rate, Q, reveals a similar decay, being proportional to $Q \propto \mathrm{Re_j}^{-2.20}$.

The investigation for a relation between the film thickness and the wall velocity contains inaccuracies due to the time required for the film to develop. Nevertheless, a relation between the film thickness and the wall velocity is found, although it is not expected to be accurate due to inaccurate measurements.

The Gerris flow solver is found to be accurate to simulate multi-phase dip coating flows containing surface tension and contact line dynamics. It does however require special attention regarding the mesh dependence of contact line dynamics. Overall, it can be concluded that film thinning using an impinging jet, reduces the flow rate of the film entrained and can hence be used to generate thinner films.

Chapter 6

Recommendations

Contact line dynamics is a challenging subject in numerical simulations, due to numerical computation of the liquid-gas interface and surface tension. As shown in the work, Gerris is capable of simulating physical simulations regarding dip coating. Also shown is the loss of accuracy in determining the front ridge due to a mesh dependence. Therefore, a valuable addition to the software would be to allow more user control regarding contact line dynamics. This would allow the use of experimental data to fine tune the contact line dynamics model.

In regard to simulations of a dip coating film impinged by a jet. Film thinning results in a film thickness of less than a cell size. This is not an issue in flat films, since the interface height calculation is accurately computed for thicknesses smaller than a cell size. It does however pose a problem near the highly curved film front, where the linear approximation used to determine the liquid-gas interface is insufficient and the surface tension implementation becomes flawed. Adopting a smaller mesh solves this issue. Note however that contact line dynamics also changes due to the mesh dependence. The problem of insufficient mesh refinement is especially relevant when performing simulation with the intent to stop film entrainment using a jet, as the liquid front curvature becomes high before the contact line velocity becomes zero.

The proportional control function used by the jet can be altered to converge faster to the desired value by multiplying the equation given in equation 4.1. Note, however, that it is a feedback system (using velocity of previous time step to determine acceleration) and multiplication by high numbers might result in an unstable system. Although this is unlikely to occur in fast systems like the one discussed, the use of a proportional control function should always be checked for oscillating outputs.

Furthermore, droplet separation at the liquid build-up prior to the jet is a fully 3D effect and should therefore be resolved in 3D models. Additionally, for high jet velocities, the jet causes waves in the film prior to the jet ($y/l_c < 10$). These waves might also propagate in the z-direction (towards the paper), which would also require the use of a 3D model.

Bibliography

[1] K. Afanasiev, A. Münch, and B. Wagner. Landau-Levich problem for non-Newtonian liquids. *Physical Review E*, vol. 76:036307, Sep 2007. 1

[2] S. Afkhami and M. Bussmann. Height functions for applying contact angles to 2D VOF simulations. *International Journal for Numerical Methods in Fluids*, vol. 57:453–472, Jun 2008. 1, 16

[3] S. Afkhami, S. Zaleski, and M. Bussmann. A mesh-dependent model for applying dynamic contact angles to VOF simulations. *Journal of Computational Physics*, vol. 228:5370–5389, Aug 2009. 16

[4] G. Agbaglah, S. Delaux, D. Fuster, J. Hoepffner, C. Josserand, S. Popinet, P. Ray, R. Scardovelli, and S. Zaleski. Parallel simulation of multiphase flows using octree adaptivity and the volume-of-fluid method. *Comptes Rendus MC*, vol. 339:194–207, Feb 2011. 15

[5] G.K. Batchelor. *An introduction to fluid dynamics.* Cambridge University Press, 1970. 7

[6] A.L. Bertozzi, A. Münch, X. Fanton, and A.M. Cazabat. Contact line stability and "undercompressive shocks" in driven thin film flow. *Physical Review Letters*, vol. 81:5169–5172, Dec 1998. 1, 12

[7] A.L. Bertozzi, A. Münch, and M. Shearer. Undercompressive shocks in thin film flows. *Physica D: Nonlinear Phenomena*, vol. 134:431–464, Oct 1999. 12

[8] B.V. Derjaguin. On the thickness of a layer of liquid remaining on the walls of vessels after their emptying, and the theory of the application of photoemulsion after coating on the cine film (presented by academician A.N. Frumkin on July 28, 1942). *Progress in Surface Science*, vol. 43:129–133, Aug 1993. 1, 10

[9] J. Eggers. Hydrodynamic theory of forced dewetting. *Physical Review Letters*, vol. 93:094502, Aug 2004. 1

[10] H.B. Eral, D.J.C.M. 't Mannetje, and J.M. Oh. Contact angle hysteresis: a review of fundamentals and applications. *Colloid Polymer Science*, vol. 291:247–260, Feb 2013. 5, 6

[11] M.M. Francois, S.J. Cummins, E.D. Dendy, D.B. Kothe, J.M. Sicilian, and M.W. Williams. A balanced-force algorithm for continuous and sharp interfacial surface tension models within a volume tracking framework. *Journal of Computational Physics*, vol. 213:141–173, Mar 2006. 16, 17

[12] P. Gennes, F. Brochard-Wyart, and D. Quéré. *Capillarity and Wetting Phenomena: Drops, Bubbles, Pearls, Waves.* Springer, New York, 2004. 3, 5, 8, 9, 12

[13] C. Huh and L. Scriven. Hydrodynamic model of steady movement of a solid/liquid/fluid contact line. *Journal of Colloid and Interface Science*, vol.35:85–101, Jan 1971. 5

[14] L. Landau and B. Levich. Dragging of a liquid by a moving plate. *Acta Physicochimica U.R.S.S.*, vol. 17:42–54, 1942. 1, 10, 12

[15] M. Maleki, E. Reyssat, D. Quéré, and R. Golestanian. On the Landau-Levich transition. *Langmuir*, vol. 23:10116–10122, Aug 2007. 1

[16] M. Maleki, M. Reyssat, F. Restagno, D. Quéré, and C. Clanet. Landau-Levich menisci. *Journal of Colloid and Interface Science*, vol. 354:359–363, Feb 2011. 1, 10, 12

[17] H.C. Mayer and R. Krechetnikov. Landau-Levich flow visualization: Revealing the flow topology responsible for the film thickening phenomena. *Physics of Fluids*, vol. 24:052103, May 2012. 1

[18] S. Popinet. Gerris: a tree-based adaptive solver for the incompressible Euler equations in complex geometries. *Journal of Computational Physics*, vol. 190:572–600, Sep 2003. 14

[19] S. Popinet. An accurate adaptive solver for surface-tension-driven interfacial flows. *Journal of Computational Physics*, vol. 228:5838–5866, Sep 2009. 1, 14, 16, 17

[20] J.H. Snoeijer and B. Andreotti. Moving contact lines: Scales, regimes, and dynamical transitions. *Annual Review of Fluid Mechanics*, vol. 45:269–292, Jan 2013. iiiiii, 12, 16

[21] J.H. Snoeijer, G. Delon, M. Fermigier, and B. Andreotti. Avoided critical behavior in dynamically forced wetting. *Physical Review Letters*, vol. 96:174504, May 2006. 1, 5, 12, 13, 21, 34

[22] S. Srivastava, J.H.M. ten Thije Boonkkamp, and F. Toschi. *Lattice Boltzmann method for contact line dynamics*. PhD thesis, Department of Applied Physics, 2014. 9

Appendix A

Meniscus rise parameter file

```
1 0 GfsSimulation GfsBox GfsGEdge { x = 0.5 y = 0.5 } {
Global {
#define u_w 1.2
#define h_i 0.5 // interface height
#define rho_g 2e-2
#define rho_l 10
#define mu_g 1.5e-5
#define mu_l 1e-2
#define gamma_l 7.2e-2
#define grav 9.81e-2
#define CA 60

// Multi-component variables
#define VAR(T,min,max) (min + CLAMP(T,0,1)*(max-min))
#define rho(T)     VAR(T,rho_g,rho_l)
#define mu(T)    VAR(T,mu_g, mu_l)
}

GfsTime { end = 200 } #dtmax=1e-4}
GfsRefine 6

# Adding liquid
VariableTracerVOFHeight T   # Used to track the interface
VariableCurvature K T     # Curvature K(appa) determined by tracer T


SourceTension T gamma_l K   # Surface tension as per tracer and curvature

# Smooths the density. Required when using large density differences
VariableFiltered T1 T 1
PhysicalParams { L = 2 }
Source V -grav
PhysicalParams { alpha = 1./rho(T1) }
SourceViscosity mu(T1)

GfsAdvectionParams { cfl = 0.5 }  # Allows the flow not to move more than half a
    gridsize

InitFraction T ( (h_i + 0.1568*exp(-8*x)- y ))



# Adaptive grid refinement
AdaptFunction { istep = 1 } { minlevel = 6 maxlevel = 10 } (T > 0 && T < 1)


GfsOutputTime { step = 0.01 } stdout
GfsOutputBalance { step = 0.01} stdout
```

```
GfsOutputProjectionStats { step = 0.01 } stdout
# GfsOutputScalarSum {step = 0.01 } stdout
# GfsOutputPPM { step = 0.002 } { ppm2mpeg > Density.mpg } { min = 0 max = 1 v = T
    }
# GfsOutputPPM { step = 0.002 } { ppm2mpeg > Velocity.mpg } { min = 0 max = 1 v = U
    }


# Temporary to determine meshing
GfsOutputSimulation { step = 0.1 } %3.2f.gfs
GfsOutputSimulation {start=0 step=0.1} CAtest-%d-%05.2f.vtk {
variables = T,U,V,P
format = VTK
precision = %.12f
}

GfsEventScript { step = 0.1 } {
  mv *.*.gfs /data/storage3/boog/LL/$(basename "${PWD}")/gfs/.
  mv *.vtk /data/storage3/boog/LL/$(basename "${PWD}")/vtk/.
  }
}
GfsBox { id = 1 pid = 0
  left = Boundary {
    BcDirichlet V 0
    BcAngle T CA
  }

  bottom = Boundary {}
  top = Boundary {
    BcDirichlet P 0
    BcNeumann V 0
  }
  right = Boundary {}
}
```

Appendix B

Dip-coating film parameter file

```
1 0 GfsSimulation GfsBox GfsGEdge { x = 0.5 y = 0.5 } {
Global {
#define u_w 0.5
#define h_i 0.85 // interface height
#define rho_g 2
#define rho_l 10
#define mu_g 1.5e-3
#define mu_l 1e-2
#define gamma_l 7.2e-2
#define grav 9.81e-2
#define CA 60

// Multi-component variables
#define VAR(T,min,max) (min + CLAMP(T,0,1)*(max-min))
#define rho(T)    VAR(T,rho_g,rho_l)
#define mu(T)   VAR(T,mu_g, mu_l)
}

GfsTime { end = 23 } #dtmax=1e-4}
GfsRefine 7

# Adding liquid
VariableTracerVOFHeight T   # Used to track the interface
VariableCurvature K T     # Curvature K(appa) determined by tracer T


SourceTension T gamma_l K   # Surface tension as per tracer and curvature

# Smooths the density. Required when using large density differences
VariableFiltered T1 T 1
PhysicalParams { L = 8 }
Source V -grav
PhysicalParams { alpha = 1./rho(T1) }
SourceViscosity mu(T1)

GfsAdvectionParams { cfl = 0.5 }  # Allows the flow not to move more than half a
    gridsize

InitFraction T ( (h_i + 0.125*exp(-8*x)- y ))

# Adaptive grid refinement
AdaptFunction { istep = 1 } { minlevel = 7 maxlevel = 11 } (T > 0 && T < 1)
AdaptFunction { istep = 1 } { minlevel = 7 maxlevel = 9 } (T > 0.5)
AdaptFunction { istep = 1 } { minlevel = 7 maxlevel = 11 } (x < 0.15)

GfsOutputTime { step = 0.01 } stdout
GfsOutputBalance { step = 0.01} stdout
GfsOutputProjectionStats { step = 0.01 } stdout
```

```
# GfsOutputScalarSum {step = 0.01 } stdout
# GfsOutputPPM { step = 0.002 } { ppm2mpeg > Density.mpg } { min = 0 max = 1 v = T
    }
# GfsOutputPPM { step = 0.002 } { ppm2mpeg > Velocity.mpg } { min = 0 max = 1 v = U
     }

# Temporary to determine meshing
GfsOutputSimulation { step = 0.01 } %3.2f.gfs
GfsOutputSimulation {start=0 step=0.01} CAtest-%d-%05.2f.vtk {
  variables = T,U,V,P
  format = VTK
  precision = %.12f
}

GfsEventScript { step = 0.01 } {
  mv *.*.gfs /data/storage3/boog/LL/$(basename "${PWD}")/gfs/.
  mv *.vtk /data/storage3/boog/LL/$(basename "${PWD}")/vtk/.
}

}
GfsBox { pid = 0
  left =  Boundary {
    BcDirichlet V ( t > 0.3 ? u_w:0 )
    BcAngle T CA
  }
  right = Boundary {}
  bottom = Boundary {}
  top = Boundary {
    BcDirichlet P 0
    BcNeumann V 0
  }
}
```

Appendix C

Dip-coating film close-up

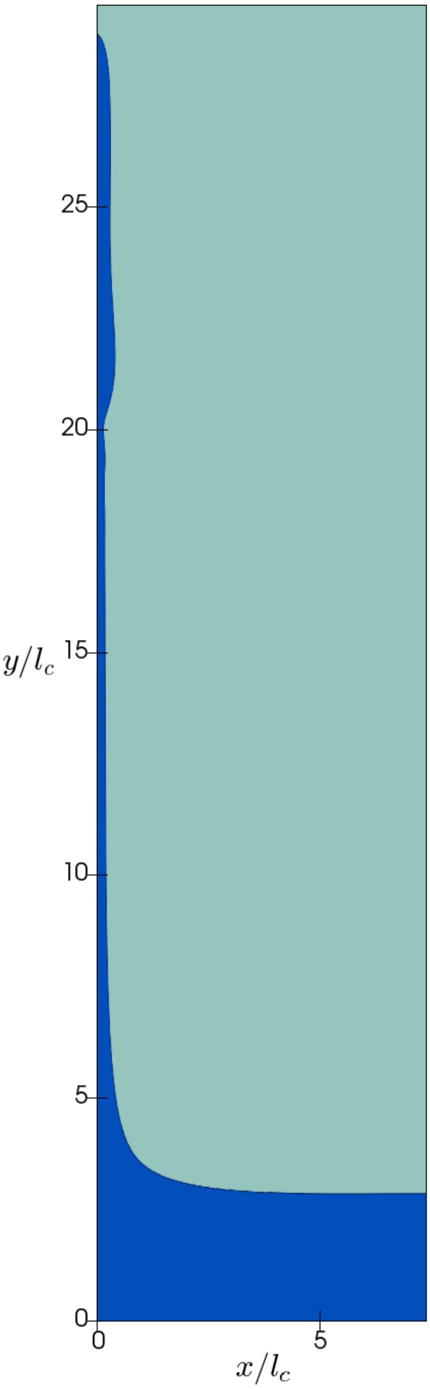

Figure C.1: Density plot close-up of the dip coating simulation result, obtained at $t = 22$s (rescaled quantity). In blue the liquid phase is shown, and in teal the gas phase.

Appendix D

Jet flow parameter file

```
1 0 GfsSimulationMoving GfsBox GfsGEdge { x = 0.5 y = 0.5 } {
Global {

#define u_j 2.5
#define h_i 0.85 // interface height
#define rho_g 2
#define rho_l 10
#define mu_g 1.5e-3
#define mu_l 1e-2
#define gamma_l 7.2e-2
#define grav 9.81e-2
#define CA 60

// Multi-component variables
#define VAR(T,min,max) (min + CLAMP(T,0,1)*(max-min))
#define rho(T)    VAR(T,rho_g,rho_l)
#define mu(T)   VAR(T,mu_g, mu_l)
}

GfsTime { end = 23 } #dtmax=1e-4}
GfsRefine 7

# First cube holds the reservoir. The second and third solids are the edges of the
    nozzle. Note that the size is taken such that the solid occupies smooth lines
    along the mesh.
#   Solid (cube(0,0.,0.,0.015625)) { tx = 1 ty = 0 sy = 150 sx = 8.1}
Solid (cube(-0.001,-0.225,0.,0.03125)) { tx = 0.6 ty = 0.513125 sy = 3 sx = 240 }
Solid (cube(-0.001,-0.138,0.,0.03125)) { tx = 0.6 ty = 0.513125 sy = 3 sx = 240 }
    # Locating cube at ty = 0.5 results in gcc error (5.1 works)


Source U ( x > 1 && y < 3.65625 && y > 3.46875 ? (u_j+U)/(0.09375*0.09375)*(y
    -3.5625)*(y-3.5625)-(u_j+U) : 0 )

# Adding liquid
VariableTracerVOFHeight T   # Used to track the interface
# VariableCurvature K T     # Curvature K(appa) determined by tracer T

# SourceTension T gamma_l K   # Surface tension as per tracer and curvature

# Smooths the density. Required when using large density differences
# VariableFiltered T1 T 1
PhysicalParams { L = 8 }
Source V -grav
PhysicalParams { alpha = 1./rho(T) }
SourceViscosity mu(T)
```

```
GfsAdvectionParams { cfl = 0.5 }  # Allows the flow not to move more than half a
    gridsize
GfsProjectionParams {
tolerance = 1e-6
nrelax    = 4
erelax    = 1
minlevel  = 0
nitermax  = 100
nitermin  = 8
}

# InitFraction T ( (h_i + 0.125*exp(-8*x)- y ))

# Adaptive grid refinement
AdaptFunction { istep = 1 } { minlevel = 6 maxlevel = 11 } (T > 0 && T < 1)
AdaptFunction { istep = 1 } { minlevel = 6 maxlevel = 8 } (T > 0.5)
AdaptFunction { istep = 1 } { minlevel = 6 maxlevel = 10 } (y > 0.75 && T > 0 && x
    < 0.6)
AdaptFunction { istep = 1 } { minlevel = 6 maxlevel = 9 } ( T > 0 && x < 0.4)
AdaptFunction { istep = 1 } { minlevel = 6 maxlevel = 11 } (y > 1. && T > 0.)
AdaptFunction { istep = 1 } { minlevel = 6 maxlevel = 8 } (x < 1.3 && (y < 5 && y >
     1.7))
AdaptFunction { istep = 1 } { minlevel = 6 maxlevel = 9 } (x < 1. && (y < 4.1 && y
    > 3))
AdaptFunction { istep = 1 } { minlevel = 6 maxlevel = 7 } (x < 7 && y < 7 )
AdaptFunction { istep = 1 } { minlevel = 6 maxlevel = 8 } (y > 3.485 && y < 3.657)
AdaptFunction { istep = 1 } { minlevel = 6 maxlevel = 9 } (y > 3.485 && y < 3.657
    && x < 1.5)

EventBalance { istep = 1 } 0.2

#    GfsOutputBoundaries {} boundaries
GfsOutputTime { step = 0.01 } stdout
GfsOutputBalance { step = 0.01} stdout
GfsOutputProjectionStats { step = 0.01 } stdout
# GfsOutputScalarSum {step = 0.01 } stdout
# GfsOutputPPM { step = 0.002 } { ppm2mpeg > Density.mpg } { min = 0 max = 1 v = T
    }
# GfsOutputPPM { step = 0.002 } { ppm2mpeg > Velocity.mpg } { min = 0 max = 1 v = U
     }


# Temporary to determine meshing
GfsOutputSimulation { step = 0.1 } %3.2f.gfs #{ variables = U,V,P }
GfsOutputSimulation {start=0 step=0.01} CAtest-%d-%05.2f.vtk {
  variables = T,U,V,P
  format = VTK
  precision = %.12f
}

GfsEventScript { step = 0.01 } {
  mv *.*.gfs /data/storage3/boog/LLjet/$(basename "${PWD}")/gfs/.
  mv *.vtk /data/storage3/boog/LLjet/$(basename "${PWD}")/vtk/.
}

}
GfsBox { pid = 0
  left =  Boundary {
    BcDirichlet V 0
    BcAngle T CA
  }
  right = Boundary {
    BcDirichlet P grav*rho_g*(8-y)
    BcNeumann P 0
    BcNeumann U 0
  }
  bottom = Boundary {}
```

```
   top = Boundary {
     BcDirichlet P 0
     BcNeumann P 0
     BcNeumann V 0
   }
}
```

Appendix E

Landau-Levich film impinged by a gas jet parameter file

```
1 0 GfsSimulationMoving GfsBox GfsGEdge { x = 0.5 y = 0.5 } {
Global {
#define u_w 1.
#define u_j 2.
#define h_i 0.85 // interface height
#define rho_g 2
#define rho_l 10
#define mu_g 1.5e-3
#define mu_l 1e-2
#define gamma_l 7.2e-2
#define grav 9.81e-2
#define CA 60

// Multi-component variables
#define VAR(T,min,max) (min + CLAMP(T,0,1)*(max-min))
#define rho(T)     VAR(T,rho_g,rho_l)
#define mu(T)    VAR(T,mu_g, mu_l)
}

GfsTime { end = 23 } #dtmax=1e-4}
GfsRefine 7

# First cube holds the reservoir. The second and third solids are the edges of the
    nozzle. Note that the size is taken such that the solid occupies smooth lines
    along the mesh.
Solid (cube(0,0.,0.,0.015625)) { tx = 1 ty = 0 sy = 150 sx = 8.1}
Solid (cube(-0.001,-0.225,0.,0.03125)) { tx = 0.6 ty = 0.513125 sy = 3 sx = 240 }
Solid (cube(-0.001,-0.138,0.,0.03125)) { tx = 0.6 ty = 0.513125 sy = 3 sx = 240 }
    # Locating cube at ty = 0.5 results in gcc error (5.1 works)

Source U ( x > 1 && y < 3.65625 && y > 3.46875 ? (u_j+U)/(0.09375*0.09375)*(y
    -3.5625)*(y-3.5625)-(u_j+U) : 0 )

# Adding liquid
VariableTracerVOFHeight T   # Used to track the interface
VariableCurvature K T     # Curvature K(appa) determined by tracer T

SourceTension T gamma_l K   # Surface tension as per tracer and curvature

# Smooths the density. Required when using large density differences
# VariableFiltered T1 T 1
PhysicalParams { L = 8 }
Source V -grav
PhysicalParams { alpha = 1./rho(T) }
SourceViscosity mu(T)
```

```
GfsAdvectionParams { cfl = 0.5 }  # Allows the flow not to move more than half a
    gridsize
GfsProjectionParams {
tolerance = 1e-6
nrelax    = 4
erelax    = 1
minlevel  = 0
nitermax  = 100
nitermin  = 8
}

InitFraction T ( (h_i + 0.125*exp(-8*x)- y ))

# Adaptive grid refinement
AdaptFunction { istep = 1 } { minlevel = 6 maxlevel = 11 } (T > 0 && T < 1)
AdaptFunction { istep = 1 } { minlevel = 6 maxlevel = 8 } (T > 0.5)
AdaptFunction { istep = 1 } { minlevel = 6 maxlevel = 10 } (y > 0.75 && T > 0 && x
    < 0.6)
AdaptFunction { istep = 1 } { minlevel = 6 maxlevel = 9 } ( T > 0 && x < 0.4)
AdaptFunction { istep = 1 } { minlevel = 6 maxlevel = 11 } (y > 1. && T > 0.)
AdaptFunction { istep = 1 } { minlevel = 6 maxlevel = 8 } (x < 1.3 && (y < 5 && y >
     1.7))
AdaptFunction { istep = 1 } { minlevel = 6 maxlevel = 9 } (x < 1. && (y < 4.1 && y
    > 3))
AdaptFunction { istep = 1 } { minlevel = 6 maxlevel = 7 } (x < 7 && y < 7 )
AdaptFunction { istep = 1 } { minlevel = 6 maxlevel = 8 } (y > 3.485 && y < 3.657)
AdaptFunction { istep = 1 } { minlevel = 6 maxlevel = 9 } (y > 3.485 && y < 3.657
    && x < 1.5)
#    AdaptFunction { istep = 1 } { minlevel= 6 maxlevel = 7 } (U > 8)

EventBalance { istep = 1 } 0.2

#    GfsOutputBoundaries {} boundaries
GfsOutputTime { step = 0.01 } stdout
GfsOutputBalance { step = 0.01} stdout
GfsOutputProjectionStats { step = 0.01 } stdout
# GfsOutputScalarSum {step = 0.01 } stdout
# GfsOutputPPM { step = 0.002 } { ppm2mpeg > Density.mpg } { min = 0 max = 1 v = T
    }
# GfsOutputPPM { step = 0.002 } { ppm2mpeg > Velocity.mpg } { min = 0 max = 1 v = U
     }


# Temporary to determine meshing
GfsOutputSimulation { step = 0.1 } %3.2f.gfs #{ variables = U,V,P }
GfsOutputSimulation {start=0 step=0.01} CAtest-%d-%05.2f.vtk {
  variables = T,U,V,P
  format = VTK
  precision = %.12f
}

GfsEventScript { step = 0.01 } {
  mv *.*.gfs /data/storage3/boog/LLjet/$(basename "${PWD}")/gfs/.
  mv *.vtk /data/storage3/boog/LLjet/$(basename "${PWD}")/vtk/.
}

}
GfsBox { pid = 0
  left =  Boundary {
    BcDirichlet V ( t > 1 ? u_w:0 )
    BcAngle T CA
  }
  right = Boundary {
    BcDirichlet P grav*rho_g*(8-y)
    BcNeumann P 0
    BcNeumann U 0
```

```
  }
  bottom = Boundary {}
  top = Boundary {
    BcDirichlet P 0
    BcNeumann P 0
    BcNeumann V 0
  }
}
```

Appendix F

Contact line velocity while passing the jet

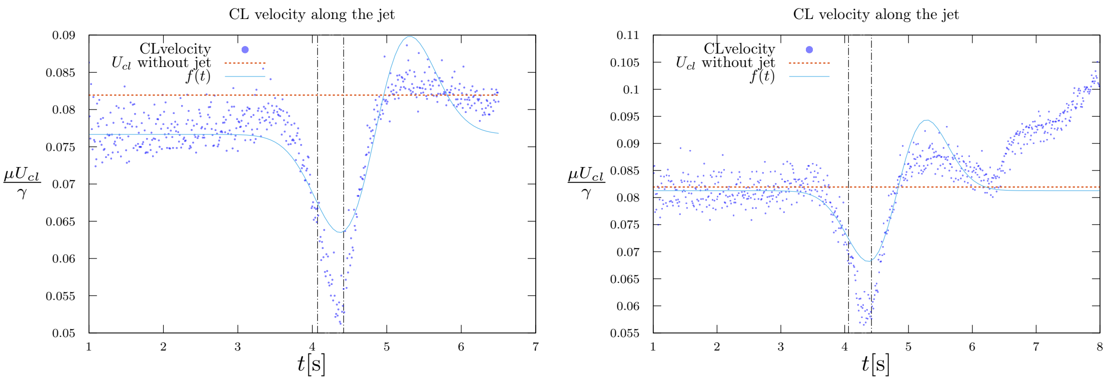

(a) $\mathrm{Re_j} \approx 53$, $0.0464(t-4.84)exp[-2.273(x-4.84)]+0.0767$

(b) $\mathrm{Re_j} \approx 56$

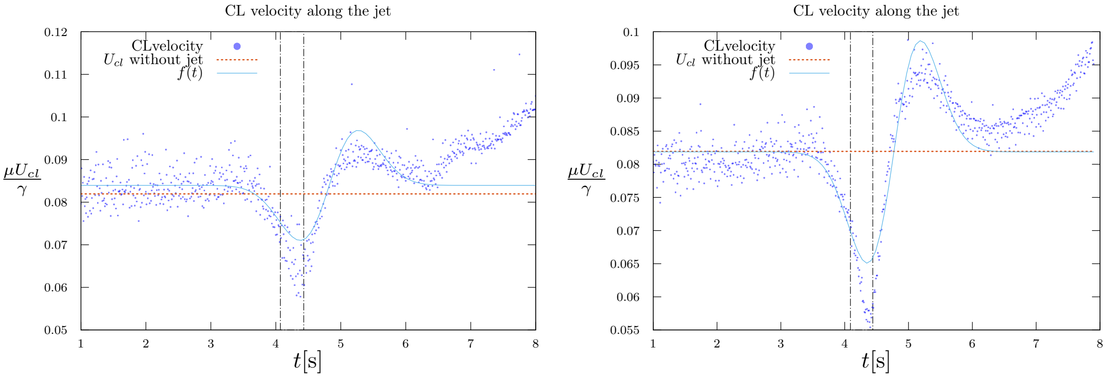

(c) $\mathrm{Re_j} \approx 59$

(d) $\mathrm{Re_j} \approx 66$

Figure F.1

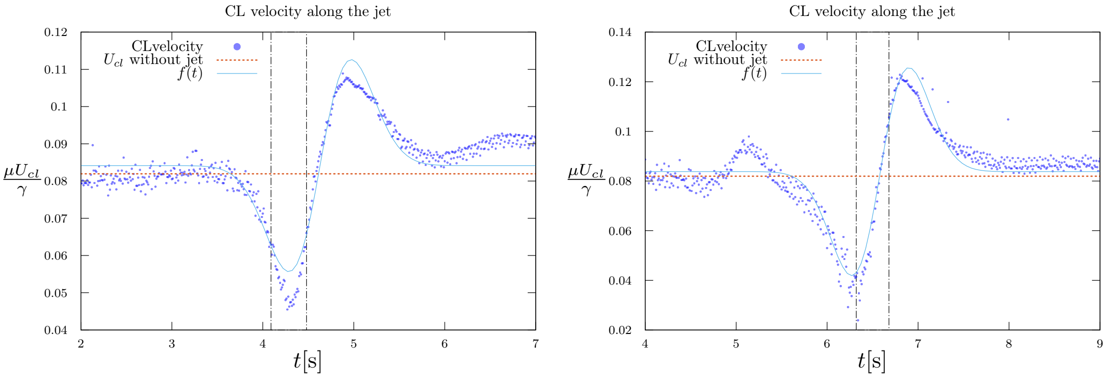

(e) $\mathrm{Re_j} \approx 79$

(f) $\mathrm{Re_j} \approx 86$

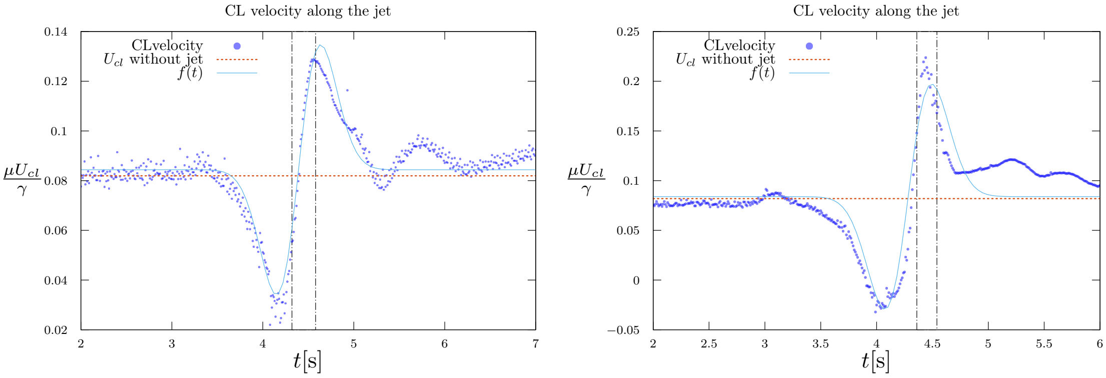

(g) $\mathrm{Re_j} \approx 112$

(h) $\mathrm{Re_j} \approx 137$

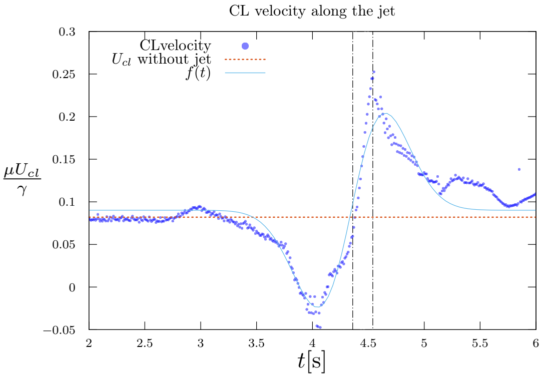

(i) $\mathrm{Re_j} \approx 153$

Figure F.1: Contact line velocity along the jet for varies jet Reynolds numbers for a fixed wall velocity, $\mathrm{Ca} = 13.9 \cdot 10^{-2}$. The fitting function is $f(t) = a(x-c)exp[b(x-c)] + d$. Fit parameters are available in Table F.1.

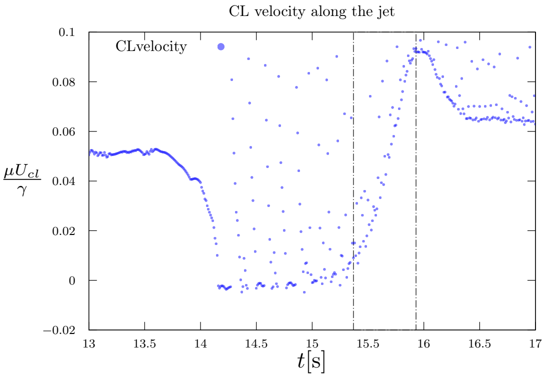

(a) $\mathrm{Ca} = 9.72 \cdot 10^{-2}$

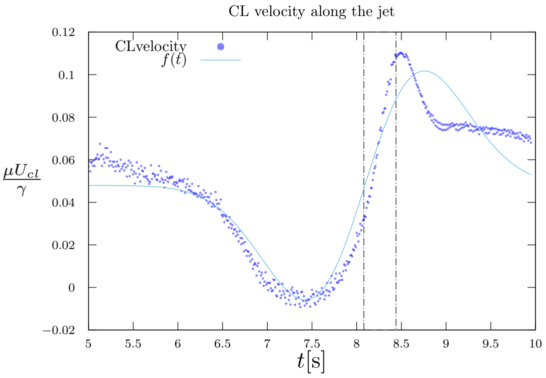

(b) $\mathrm{Ca} = 11.1 \cdot 10^{-2}$

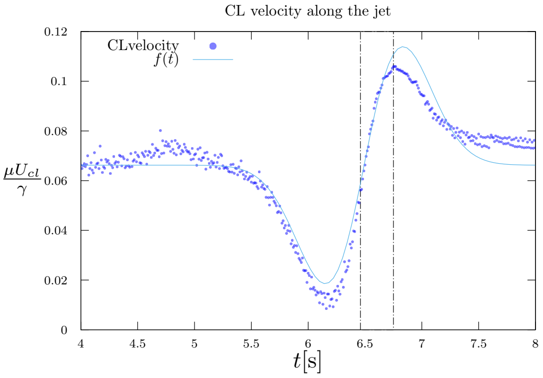

(c) $\mathrm{Ca} = 12.5 \cdot 10^{-2}$

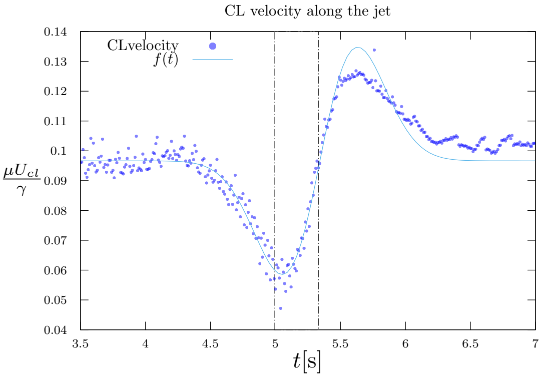

(d) $\mathrm{Ca} = 15.3 \cdot 10^{-2}$

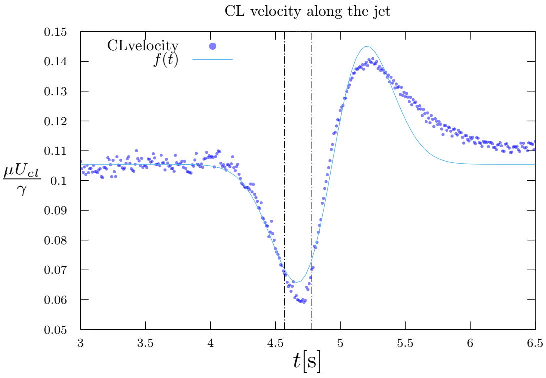

(e) $\mathrm{Ca} = 16.7 \cdot 10^{-2}$

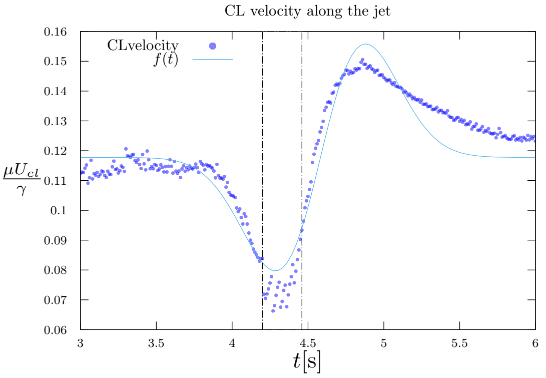

(f) $\mathrm{Ca} = 18.1 \cdot 10^{-2}$

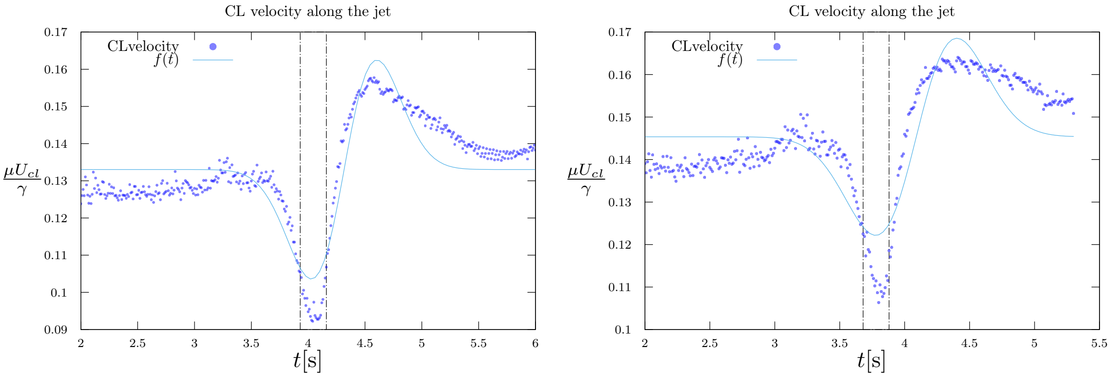

(g) $\mathrm{Ca} = 19.4 \cdot 10^{-2}$ (h) $\mathrm{Ca} = 20.8 \cdot 10^{-2}$

Figure F.2: Contact line velocity along the jet for varies wall capillary numbers with a fixed jet Reynolds number, $\mathrm{Re_j} \approx 86$. The fitting function is $f(t) = a(x-c)exp[b(x-c)]+d$. Fit parameters are available in Table F.2.

Table F.1: Fit parameters corresponding to Figure F.1.

$\mathrm{Re_j}$	a	b	c	d	$\sigma^2 \cdot 10^{-5}$
53	0.0464	2.27	4.84	0.0767	1.40
56	0.0472	2.40	4.83	0.0813	2.10
59	0.0477	2.50	4.82	0.0839	2.07
66	0.0662	2.86	4.78	0.0819	1.12
69	0.123	3.43	5.67	0.0829	1.52
79	0.137	4.25	4.69	0.0841	1.71
86	0.219	5.03	6.58	0.0838	2.80
112	0.341	8.46	4.39	0.0840	2.93
137	0.891	11.4	4.28	0.0839	38.2
153	0.619	5.43	4.35	0.0901	28.9

Table F.2: Fit parameters corresponding to Figure F.2.

Ca $\cdot 10^{-2}$	a	b	c	d	$\sigma^2 \cdot 10^{-5}$
9.72	0.0883	1.09	15.5	0.0474	33.0
11.1	0.133	1.13	8.09	0.048	10.3
12.5	0.230	4.27	6.49	0.0662	3.65
15.3	0.216	5.93	5.34	0.0966	1.25
16.7	0.244	6.93	4.94	0.105	1.04
18.1	0.211	5.65	4.58	0.118	3.67
19.4	0.168	6.02	4.32	0.133	3.61
20.8	0.123	5.13	4.09	0.145	4.65

Appendix G

Flow rate of thinned films

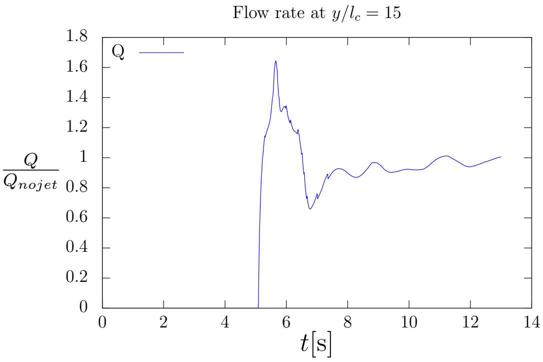

(a) $\mathrm{Re_j} \approx 53$

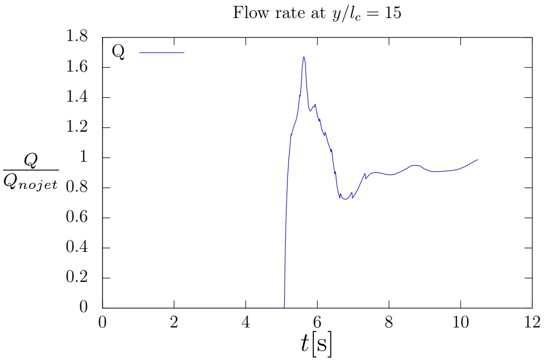

(b) $\mathrm{Re_j} \approx 56$

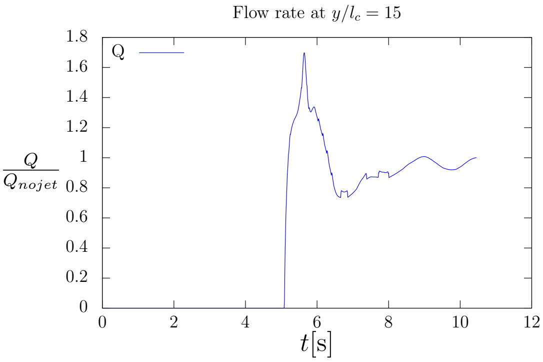

(c) $\mathrm{Re_j} \approx 59$

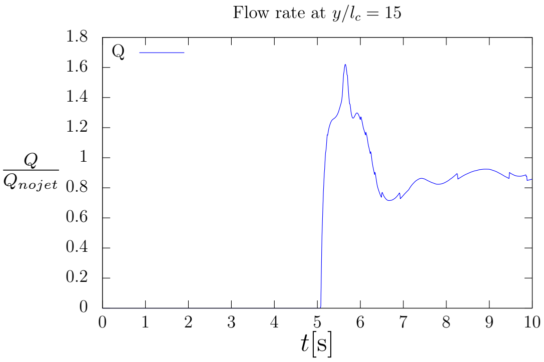

(d) $\mathrm{Re_j} \approx 61$

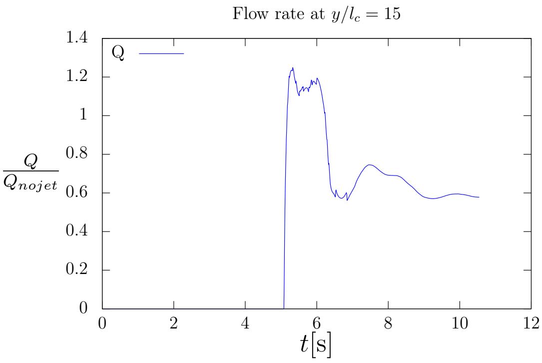

(e) $\mathrm{Re_j} \approx 66$

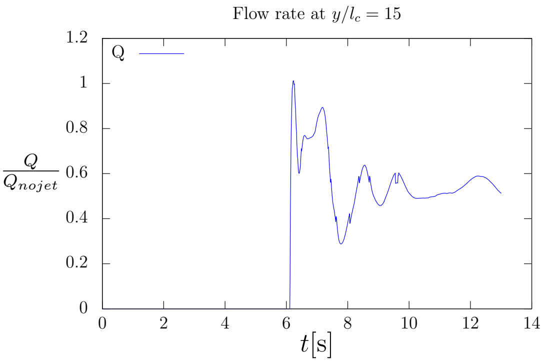

(f) $\mathrm{Re_j} \approx 69$

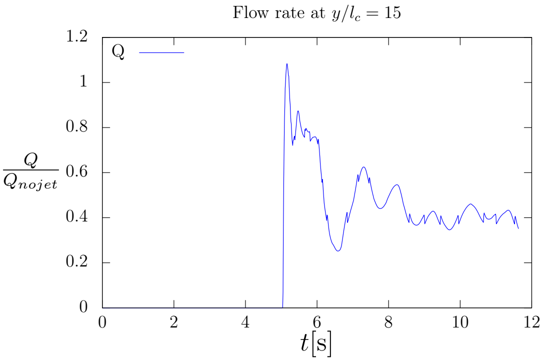

(g) $\mathrm{Re_j} \approx 79$

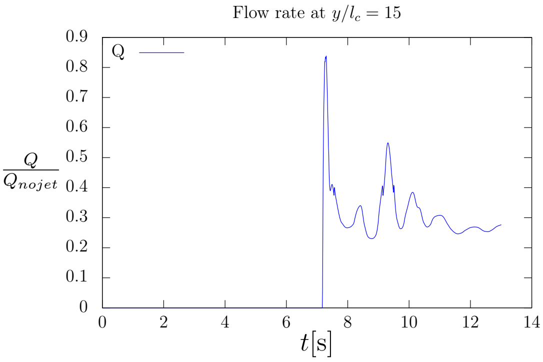

(h) $\mathrm{Re_j} \approx 86$

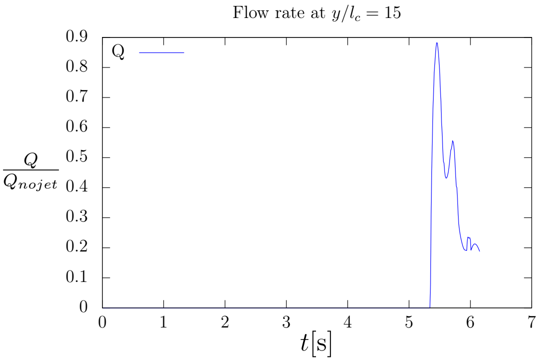

(i) $\mathrm{Re_j} \approx 103$

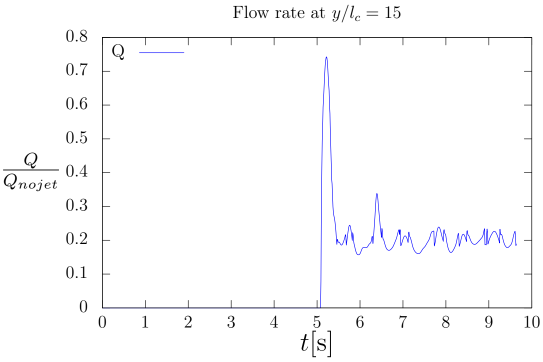

(j) $\mathrm{Re_j} \approx 112$

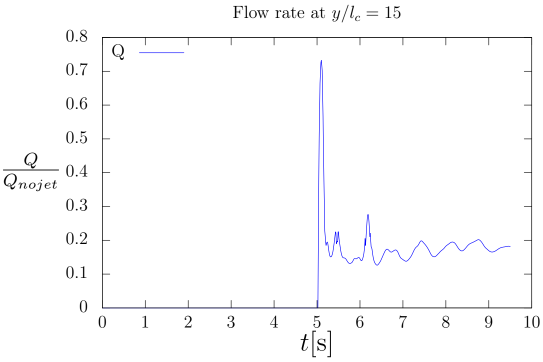

(k) $\mathrm{Re_j} \approx 120$

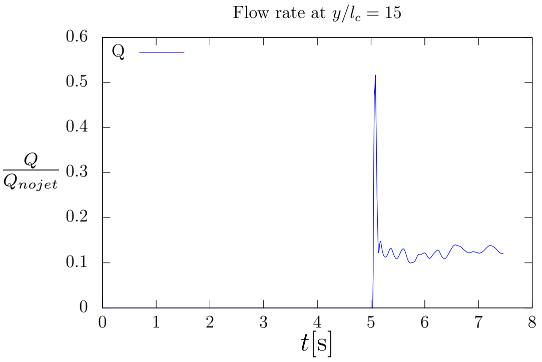

(l) $\mathrm{Re_j} \approx 137$

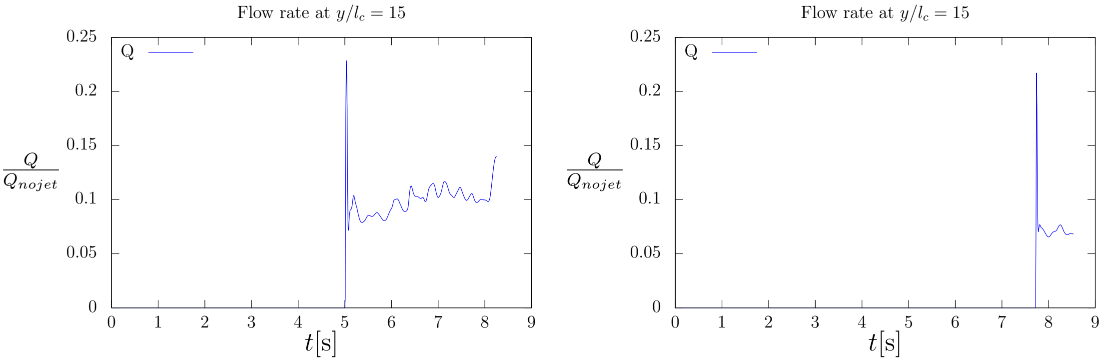

(m) $\mathrm{Re_j} \approx 153$ (n) $\mathrm{Re_j} \approx 169$

Figure G.1: Flow rate for different jet velocities and a fixed wall velocity, $\mathrm{Ca} = 13.9 \cdot 10^{-2}$. Measured at a fixed position of $y/l_c = 15$. Normalized by $Q_{nojet} = 4.31 \cdot 10^{-2}\mathrm{m}^2/\mathrm{s}$ (scaled), the flow rate at $y/l_c = 15$ without an impinging jet.